Distinct evolution of SARS-CoV-2 Omicron XBB and BA.2.86/JN.1 lineages combining increased fitness and antibody evasion

Delphine Planas[1,2*], Isabelle Staropoli[1], Vincent Michel[3], Frederic Lemoine[4,5], Flora Donati[4,6], Matthieu Prot[4], Francoise Porrot[1], Florence Guivel-Benhassine[1], Banujaa Jeyarajah[6], Angela Brisebarre[6], Océane Dehan[6], Léa Avon[6], William Henry Boland[1], Mathieu Hubert[1], Julian Buchrieser[1], Thibault Vanhoucke[1], Pierre Rosenbaum[7], David Veyer[8,9], Hélène Péré[8,9], Bruno Lina[10,11], Sophie Trouillet-Assant[10,11] on behalf of COVID-SER study group, Laurent Hocqueloux[12], Thierry Prazuck[12], Etienne Simon-Loriere[4,6*,$], Olivier Schwartz[1,2*,$].

[1] Virus and Immunity Unit, Institut Pasteur, Université Paris Cité, CNRS UMR3569, Paris, France.
[2] Vaccine Research Institute, Créteil, France.
[3] Pathogenesis of Vascular Infections Unit, Institut Pasteur, INSERM, Paris, France.
[4] G5 Evolutionary Genomics of RNA Viruses, Institut Pasteur, Université Paris Cité, Paris, France.
[5] Bioinformatics and Biostatistics Hub, Paris, France.
[6] National Reference Center for Respiratory Viruses, Institut Pasteur, Paris, France.
[7] Humoral Immunology Laboratory, Institut Pasteur, Université Paris Cité, INSERM U1222, Paris, France.
[8] Laboratoire de Virologie, Service de Microbiologie, Hôpital Européen Georges Pompidou, Paris, France.
[9] Functional Genomics of Solid Tumors (FunGeST), Centre de Recherche des Cordeliers, INSERM, Université de Paris, Sorbonne Université, Paris, France.
[10] Laboratoire de Virologie, Institut des Agents Infectieux, Centre National de Référence des virus des infections respiratoires, Hospices Civils de Lyon, Lyon, France.
[11] CIRI, Centre International de Recherche en Infectiologie, Team VirPath, Univ Lyon, Inserm, U1111, Université Claude Bernard Lyon 1, CNRS, Lyon, France.
[12] CHU d'Orléans, Service de Maladies Infectieuses, Orléans, France.

[*]Co-corresponding authors
delphine.planas@pasteur.fr; etienne.simon-loriere@pasteur.fr and olivier.schwartz@pasteur.fr
[$] co-last authors

Abstract

The unceasing circulation of SARS-CoV-2 leads to the continuous emergence of novel viral sublineages. Here, we isolated and characterized XBB.1, XBB.1.5, XBB.1.9.1, XBB.1.16.1, EG.5.1.1, EG.5.1.3, XBF, BA.2.86.1 and JN.1 variants, representing >80% of circulating variants in January 2024. The XBB subvariants carry few but recurrent mutations in the spike, whereas BA.2.86.1 and JN.1 harbor >30 additional changes. These variants replicated in IGROV-1 but no longer in Vero E6 and were not markedly fusogenic. They potently infected nasal epithelial cells, with EG.5.1.3 exhibiting the highest fitness. Antivirals remained active. Neutralizing antibody (NAb) responses from vaccinees and BA.1/BA.2-infected individuals were markedly lower compared to BA.1, without major differences between variants. An XBB breakthrough infection enhanced NAb responses against both XBB and BA.2.86 variants. JN.1 displayed lower affinity to ACE2 and higher immune evasion properties compared to BA.2.86.1. Thus, while distinct, the evolutionary trajectory of these variants combines increased fitness and antibody evasion.

Introduction

Succeeding sub-lineages of Omicron have spread since the appearance of BA.1 in November 2021 [1,2]. More than 90% of the human population have been probably infected by one Omicron subvariant, in the absence of an efficient and long-lasting protection against novel viral acquisitions conferred by previous infections or vaccinations [3-6], allowing the virus to further evolve and diversify. Identified in September 2022, the XBB lineage originated from a recombination of two BA.2-derived variants (BJ.1 and BM.1.1.1) and progressively replaced most of previous Omicron strains. Members of this lineage are characterized by enhanced transmissibility rates and immune evasion properties [7,8]. These variants are responsible for small waves of contaminations in many countries. Their geographical distribution is somewhat heterogeneous. The variants are closely related and carry an additional and limited set of mutations in the spike corresponding to a stepwise accumulation of changes. Convergent evolution may have been associated with this process. For instance, many lineages independently acquired mutations in the Receptor Binding Domain (RBD) of the spike, including F486P or F456L, that are known escape mutations for neutralizing antibodies [9] [10]. Other recombinants increased in frequency in regions of the world but did not spread extensively, for example XBF (a recombinant of BA.5.2.3 and BA.2.75.3 lineages) or XBC (a recombinant of BA.2 and Delta lineages), both noted in Australia or New Zealand and carrying the F486P substitution. This convergent evolution is likely due to a similar selective pressure exerted by imprinted or hybrid immunity triggered by Omicron infection and/or vaccination [11-14].

In August 2023, a lineage named BA.2.86 corresponding to an important evolutionary jump has been detected in multiple countries, prompting its classification as a Variant of Interest by the World Health Organization [15]. The effective reproduction number of BA.2.86 is estimated to be higher or similar than those of XBB.1.5 and EG.5.1 [16]. A high attack rate of BA.2.86 (above 85%) occurred in a large care home outbreak, confirming its high transmissibility [17]. There is so far no clinical evidence of increased pathogenicity of BA.2.86. In hamsters, BA.2.86 displays an attenuated phenotype [18 19,20]. The impact of this unprecedented combination of mutations on antibody evasion has started to be deciphered. A few recent articles and preprints reported that NAb responses to BA.2.86 are lower than BA.2, but comparable or slightly higher than to other simultaneously circulating XBB-derived variants [16,21-31,20]. Most of these studies were performed with lentiviral or VSV pseudotypes. Isolation of a BA.2.86 virus confirmed the antibody-escape properties of this strain [20,25]. BA.2.86 spike displays stronger affinity to ACE2 than other variants [31 29 28], but the consequences on viral replication and tropism remain poorly understood.

The BA.2.86 lineage has then rapidly started to evolve, with the emergence of the JN.1 sub-lineage in September 2023. In December 2023, JN.1 sharply increased in frequency in Europe and USA. It became predominant worldwide and was the main variant responsible for the epidemic surge in December 2023-January 2024. Based on epidemiological modelling, it has been estimated that JN.1 displays a 2.3-fold growth advantage relative to EG.5.1.1 [32]. A preprint using JN.1 pseudotypes reported enhanced immune evasion properties, particularly to class 1 neutralizing antibodies, associated with a decreased affinity to ACE2, relative to BA.2.86 [33].

Here, we isolated and characterized 9 viral strains that were circulating late 2023-early 2024. We performed a side-by-side comparison of their replication in cell lines and relevant human primary nasal epithelial cells, their binding to ACE2 and fusogenicity. We examined their sensitivity to previously approved mAbs and antiviral drugs, to sera from recipients of various vaccine regimens, and to individuals who experienced breakthrough infections during XBB circulation.

Results

Mutations in XBB-derived and BA2.86 spike sequences

XBB variants replaced previously circulating Omicron variants in early 2023 and have been continuously evolving. In October 2023, the main XBB sub-variants, representing about 80% of reported viral sequences, were XBB.1.5, XBB.1.9.1, XBB.1.16, XBB.2.3 and the EG.5.1 sublineage (Fig. 1a). EG.5.1 is a descendant of XBB.1.9.2 that was designated in May 2023 and has since then been on the rise [34]. The set of the spike mutations is depicted Fig. 1b and the resulting phylogenetic tree is displayed Fig. S1a. In addition to the R346T and N460K substitutions, these most frequent XBB lineages independently acquired the S486P substitution. Other substitutions were noted at this position in

110 previous variants, such as 486V in BA.5 (Fig. S1b). These variants have spread worldwide, with local
111 variations in frequency. The subsequent sequential acquisition of the F456L substitution has been
112 repeatedly noted in 486P carrying XBB lineages, suggesting an epidemiological advantage for their
113 combination in this genomic background. More than 65% of genomes shared on GISAID in October
114 2023 carry both F486L and F456L substitutions.

115 In contrast to the steady accumulation of substitutions observed in XBB sublineages, the
116 evolutionary processes that led to the emergence of BA.2.86 have not been captured. BA.2.86 spike
117 carries a novel and distinct constellation of changes. This leads to a novel branch in the SARS-CoV-2
118 spike phylogenetic tree (Fig. S1a). Compared with its BA.2 ancestor, the spike contains 34 changes, a
119 number comparable to the difference between the initial Wuhan virus and BA.1, including novel
120 insertions, deletions, and substitutions spanning the whole protein (Fig. 1b). Some mutations, such as
121 G446S, N460K, F486P, and R493Q have been reported in other variants [7 35 8] (Fig. S1b), but others are
122 less frequent and poorly characterized. Furthermore, BA.2.86 has been quickly diversifying as it
123 spreads. BA2.86.1 is characterized by two novel mutations in ORF1. JN.1 carries one additional amino
124 acid substitution (F455S) in the spike (Fig. S1b) along with the ORF1a:R3821K and ORF7b:F19L changes
125 (Fig. S2).

126

127 **Isolation of 9 variants circulating in late 2023-early 2024.**

128 We isolated XBB.1, XBB.1.5, XBB.1.9.1, XBB.1.16.1, XBF, EG.5.1.1, EG.5.1.3, BA.2.86.1 and JN.1
129 variants from nasopharyngeal swabs received at the French National Reference Center of Respiratory
130 viruses (Paris, Lyon) and Hôpital Européen Georges Pompidou (Paris, France), using either a Vero E6
131 TMPRSS2+ clone (thereafter termed Vero E6 TMP-2 cells) or IGROV-1 cells. We reported that the
132 IGROV-1 human ovarian cell line is highly sensitive to SARS-CoV-2 and produces high levels of infectious
133 virus [36]. After isolation, the 9 viruses were thus amplified by one passage on IGROV-1 cells. The
134 sequences of the variants after amplification were identical to those obtained from the primary
135 samples (see GISAID accession numbers in Table S3), indicating that no mutations occurred during this
136 short culture period. The spike mutations in these 9 variants, compared to BA.2, are depicted in Fig.
137 1b. We also compared the spike mutations of a larger panel of variants to the Wuhan ancestral strain
138 in Fig. S1b.

139

140 **Replication of XBB-derived, BA2.86.1 and JN.1 variants in Vero E6 derivatives and IGROV-1**
141 **cells.**

142 We characterized the fitness of the 9 variants by assessing their replication in different cells and
143 adding as controls D614G, BA.1, BA.5 or BQ.1.1. Since JN.1 was isolated later than the other variants,
144 it was included in most but not all experiments. We first chose Vero E6 and IGROV-1 cells, that both

145 naturally express ACE2, but not TMPRSS2, the protease that primes SARS-CoV-2 for fusion, as verified
146 by flow cytometry (Fig. S3). Vero E6 cells efficiently replicate pre-Omicron strains but are less sensitive
147 to previous Omicron variants [36]. We thus compared the permissibility of Vero E6 and IGROV-1 cells to
148 all variants (Fig. S4a). Viral stocks were serially diluted and incubated with the two target cells. After
149 48h, cells were stained with an anti-SARS-CoV-2 N monoclonal antibody. Foci of infected cells were
150 automatically scored (Fig. S4b). The ancestral D614G strain was similarly infectious in the two cell lines
151 (Fig. S4). In contrast, none of the 12 Omicron variants efficiently infected Vero E6 whereas they were
152 highly infectious in IGROV-1. We then asked whether the poor infectivity of the variants in Vero E6 was
153 due to the lack of TMPRSS2. We thus selected two Vero E6 subclones engineered to express TMPRSS2.
154 The first clone (termed Vero E6 TMP-1) was generated in our laboratory [36] and expresses high levels of
155 TMPRSS2 and rather low levels of ACE2, probably because this receptor can be cleaved by the
156 protease[37] (Fig. S3). The Vero E6 TMP-2 was previously described [38]. It expresses low surface levels of
157 TMPRSS2 and ACE2 levels comparable to those in Vero E6 cells (Fig. S3). We thus compared the kinetics
158 of viral replication in IGROV-1, Vero E6, Vero E6-TMPRSS2 clones 1 and 2. We used Delta and BQ.1.1
159 as controls (a BA.5-derived Omicron variant), and compared them to XBB.1, XBB.1.5, EG.5.1.3 and
160 BA.2.86.1 (Fig. 2a). All viruses efficiently replicated in IGROV-1 cells, with a peak of infected cells
161 detected at day 2 post infection (p.i.). The Omicron variants did not potently infect Vero E6 during the
162 4-day survey period. The two Vero E6-TMPRSS2 clones behaved differently regarding their sensitivity
163 to variants. Vero E6 TMP-1 did not support strong replication of Omicron variants, despite allowing
164 growth of Delta. In contrast, Vero E6 TMP-2 efficiently replicated the novel variants (Fig. 2a). The
165 differences between Vero E6 TMP-1 and TMP-2 might be due to clonal effects. Alternatively, high levels
166 of TMPRSS2, and reduced surface expression of ACE2 in Vero E6 TMP-1 might be detrimental for XBB-
167 derived and BA.2.86.1 variants. Regardless of the underlying mechanisms, our results indicate that the
168 recent XBB-derived and BA.2.86 variants display a different tropism than pre-Omicron viruses for some
169 cell lines. Low expression of TMPRSS2 in Vero E6 cells is associated with permissibility of the cells to
170 XBB-derived and BA.2.86.1 infection.

171 We further explored the mechanisms underlying the high sensitivity of IGROV-1 to SARS-CoV-2
172 replication. We examined viral entry pathways in these cells and performed infections in presence of
173 either Camostat, a TMPRSS2 inhibitor, SB412515, a cathepsin L inhibitor, or E-64d, a pan-cysteine
174 protease inhibitor acting mainly on endocytic proteases [39 40]. The drugs were added 2 h before infection
175 and maintained for 24 h, before scoring infected cells (Fig. S5). We first selected a few pre-Omicron
176 and recent Omicron variants, (D614G, Delta, BA.1, XBB.1 and XBB.1.16.1) and tested the effect of the
177 drugs in IGROV-1, Vero E6 and Vero TMP-1 cells. Camostat (100 µM) did not inhibit viral replication in
178 IGROV-1 and Vero E6 cells, in line with the absence of detection of TMPRSS2 in these cells by flow
179 cytometry. Camostat inhibited viral replication by 50-80% in Vero E6 TMP-1 cells, confirming that

180 TMPRSS2 facilitates viral entry when present in target cells. There was no significant difference in the
181 sensitivity of variants to Camostat in Vero E6 TMP-1 cells. SB412515 and E-64d (both at 10 µM) strongly
182 inhibited viral infections in IGROV-1 cells (>90% inhibition for all variants) but were less efficient in
183 Vero E6 cells (Fig. S5). This suggests that endocytic viral entry is particularly active in IGROV-1. With
184 both SB412515 and E-64d, similar ED50 were obtained for D614G, XBB.1.5, EG.5.1.3 and BA.2.86.1
185 variants, which may indicate that all variants use similar entry pathways in IGROV-1 cells (Fig. 2b). In
186 contrast to their strong antiviral effect in IGROV-1 and lower activity in Vero E6 cells, SB412515 and E-
187 64d were almost inactive in Vero E6 TMP-1 cells, confirming that when TMPRSS2 is present, viral entry
188 and fusion preferentially occurs at the cell surface [39 41]. We then assessed the sensitivity of Delta,
189 BA.2.86.1 and JN.1 to Camostat (100 µM), SB412515, and E-64d (10 µM) in IGROV-1 and Vero E6 TMP-
190 2 cells. SB412515 and E-64d effectively inhibited the replication of the three variants in IGROV-1 cells.
191 Camostat inhibited the replication of Delta, BA.2.86.1 and JN.1 in Vero E6 TMP-2 cells, but not in
192 IGROV-1 cells, confirming the results observed with the other variants (Fig. S6).
193 Therefore, IGROV-1 are highly sensitive to all SARS-CoV-2 strains, likely because of a strong
194 endocytic pathway facilitating viral entry.
195
196 **Fusogenicity and ACE2 binding of XBB-derived and BA2.86.1 variants.**
197 We next investigated the fusogenicity of the spikes and their ability to form syncytia
198 independently of viral replication. We used a GFP-Split based model in which fused cells become GFP+
199 (Fig. 3a) [42 43]. We transfected the spikes into 293T cells expressing the GFP-11 subunit and co-cultivated
200 them with IGROV-1 cells expressing the GFP1-10 subunit (Fig. 3a). Spike expression on transfected
201 HEK293T cells was similar across variants, as measured by staining with a pan-coronavirus anti-S2 mAb
202 (Fig. S7). As previously reported by us and others, the ancestral D614G and Delta strains were more
203 fusogenic than the early Omicron BA.1 and BA.4/5 variants [44 36 40 45]. BQ.1.1 and XBB.1.5/XBB.1.9.1
204 spikes partially regained fusogenicity, whereas XBB.1.16.1 and the more recent EG.5.1.1 and BA.2.86.1
205 spikes displayed a lower fusogenic potential than BA.4/5 spike (Figure 3b,c). This profile of fusogenicity
206 was similarly observed when Vero E6 cells were used as targets (Fig. 3d). With Vero E6 TMP-1 as target
207 cells, the number of syncytia was increased by about 2-fold for all variants, when compared to Vero E6
208 cells (Fig. 3d), indicating that TMPRSS2 enhances their fusogenic activity. Thus, the recent XBB-derived
209 and BA.2.86.1 variant spikes do not display high fusion properties, when compared to Delta or to their
210 Omicron predecessors, at least in the cell lines tested.
211 We next examined the affinity of the different variant spikes to ACE2. To this aim, we infected
212 IGROV-1 cells with most of the variants for 24h. Cells were stained with an anti-N antibody to visualize
213 productively infected cells and were exposed to serial dilutions of soluble biotinylated ACE2. Binding
214 was measured by flow cytometry (Fig. S8a). ACE2 titration binding curves were generated, and EC50

215 (the amount of ACE2 needed for 50% binding) was calculated (Fig. S8b). The spikes of XBB.1, XBB.1.16.1
216 and EG.5.1.3 had comparable affinities to ACE2 than Delta, whereas BA.2.86.1 bound more potently
217 to the receptor (Fig. 3e). Similar results were observed in 293T cells transiently expressing the different
218 spikes (Fig. 3f), confirming recent reports obtained with recombinant proteins [29] [28].
219
220 **Replication of XBB-derived and BA2.86.1 variants in primary nasal epithelial cells.**
221 We used primary nasal epithelial cells (hNEC) grown over a porous membrane and
222 differentiated at the air–liquid interface for 4 weeks (from MucilAirB™), to compare the different
223 variants in a relevant model of SARS-CoV-2 infection [46] [47] [45]. The cells were infected with each variant
224 at a similar low viral inoculum (100 µl of viral stocks containing $2x10^3$ infectious units/ml). As reported
225 [46,48] [45] [44], BA.1 replicated faster than Delta and D614G, as quantified by viral RNA (vRNA) release
226 monitored every day up to 4 days pi (Fig. 4a, b). Compared to Delta, BA.1 displayed up to 60-fold
227 increase in vRNA levels measured at 24 h pi. The XBB-derived variants exhibited a replication
228 advantage compared to BA.1, with EG.5.1.3 displaying a 16-fold increase in vRNA release at 24 h.
229 BA.2.86.1 replication kinetics resembled those of BA.1 and were not higher than other XBB-derived
230 variants (Fig. 4a, b). Infectious virus release was monitored at 48 h p.i. (Fig. 4c) and correlated with
231 vRNA levels. We assessed by immunofluorescence the cytopathic effect induced by the variants.
232 Infected hNEC were stained at day 4 p.i. with anti-SARS-CoV-2 N antibodies, phalloidin (to visualize F-
233 actin), anti-alpha tubulin antibodies (to visualize cilia) and anti-cleaved caspase 3 antibodies (to
234 visualize apoptotic dying cells). When compared to Delta or BA.1, EG.5.1.3 and BA.2.86.1 displayed
235 elevated markers of cytopathy, including disappearance of the ciliated structure and activation of
236 caspase 3 (Fig. 4d; Fig. S9).
237 Therefore, Omicron variants, particularly BQ.1.1 and XBB-derived isolates, exhibit higher
238 infectivity in hNECs compared to D614G and Delta. Among them, EG.5.1.3 demonstrates the highest
239 fitness. Additionally, both EG.5.1.3 and BA.2.86.1 variants exhibit significant cytopathic effects in these
240 cells (Fig. S9).
241
242 **Sensitivity of XBB-derived, BA2.86.1 and JN.1 variants to antiviral antibodies and small**
243 **molecules.**
244 Several anti-spike monoclonal antibodies (mAbs) have been used as pre- or post-exposure
245 therapy in individuals at risk for severe disease [10]. However, the first Omicron variants BA.1, BA.2 and
246 BA.5 escaped neutralization from most of the mAbs, leading to changes in treatment guidelines [49]. For
247 instance, as of mid-2022 and later, Ronapreve (Imdevimab + Casirivimab) or Evusheld (Cilgavimab +
248 Tixagevimab) cocktails and Sotrovimab were no longer approved [49]. However, Sotrovimab retains some
249 neutralizing and non-neutralizing Fc-mediated functions against BQ.1.1 and XBB.1.5 [50]. We assessed

250 with the S-Fuse assay the sensitivity of D614G, XBB.1.16.1, EG.5.1.3, BA.2.86.1 and JN.1 to Ronapreve,
251 Evusheld or Sotrovimab. We included the ancestral D614G strain as a control, which was efficiently
252 neutralized by the mAbs (Fig. 5). Evusheld and Ronapreve combinations were inactive against the
253 recent variants. Sotrovimab remained weakly functional against XBB.1.16.1 and EG.5.1.3 but lost
254 antiviral activity against BA.2.86.1 and JN.1. We examined whether the neutralization profile of
255 Sotrovimab correlated with the ability of the mAb to bind the different spikes. We measured by flow
256 cytometry the binding of Sotrovimab to IGROV-1 cells infected with the corresponding variants (Fig.
257 S10a,b). Cells were stained with the pan coronavirus S2 antibody mAb10 as a control (Fig. S10c). The
258 levels of binding with the different antibodies were quantified (Fig. S10d). Sotrovimab bound to all
259 XBB-derived variants but not to BA.2.86.1. This is likely due to the presence of the K356T mutation in
260 BA.2.86.1 RBD, that has been identified as conferring resistance to Sotrovimab [51 52].
261 We then assessed the efficacy of the currently approved anti-SARS-CoV-2 drugs Nirmatrelvir
262 (present in Paxlovid), Remdesivir and Molnupiravir against D614G, XBB.1.5.1, EG.5.1.3 and BA.2.86.1.
263 IGROV-1 cells were exposed to serial dilutions of the compounds, exposed to the variants, and
264 infection was revealed after 24 h (Fig. S5b). The antiviral molecules remained active against the tested
265 variants, with no significant differences in their EC50 (10 nM, 3.4 µM and 0.04 nM for Nirmatrelvir,
266 Molnupiravir and Remdesivir, respectively).
267
268 **Cohort design**
269 We collected 75 sera from two different cohorts representing a total of 41 vaccinated and/or
270 infected individuals. The characteristics of the participants (dates of vaccination, breakthrough
271 infection and sampling) are indicated in Table S1.
272 The first cohort includes two groups of individuals. The first group is composed of 21 health-care
273 workers, in Orleans, France (Table S1a). The participants received two doses of Pfizer BNT162b2
274 vaccine and one or two booster doses with the same monovalent vaccine. 13 out of 21 individuals
275 experienced a pauci-symptomatic breakthrough infection after the third injection. We did not
276 generally identify the Omicron subvariant responsible for the breakthrough infections. 13 individuals
277 were infected between December 2021 and mid-June 2022, a period when BA.1 and BA.2 were
278 successively dominant in France [53]. One individual was infected in August 2022 and was likely positive
279 for BA.5. All individuals received a Bivalent Wuhan/BA.5 Pfizer boost between December 2022 and
280 February 2023. The second group includes 12 vaccinated health-care workers, in Orleans, France, that
281 experienced a breakthrough Omicron infection in August/September 2023, when XBB-derived variants
282 were predominant (Table S1c).
283 The second cohort includes 8 health-care workers, in Lyon, France, that were longitudinally
284 sampled at day 0, one month and 6 months after their Bivalent Wuhan/BA.5 Pfizer boost (Table S1b).

285

286 **Sensitivity of XBB-derived and BA2.86.1 variants to sera from vaccinees.**

287 We assessed the sensitivity of the panel of XBB-derived and BA2.86.1 variants to serum
288 samples from the two cohorts. We first asked whether antibodies elicited by three doses of the original
289 Pfizer vaccine neutralized the novel subvariants. Twenty-one individuals were analyzed 12 months post
290 third dose (Tables S1a,bS2a). Among them, 12 individuals experienced a BA.1/BA.2 breakthrough
291 infection. We measured the potency of their sera against BQ.1.1, XBB.1, XBB.1.5; XBB.1.9.1,
292 XBB.1.16.1, XBF, EG.5.1.3 and BA.2.86.1. We used as reference the D614G ancestral strain, as well as
293 BA.1 and BA.5 (Fig. 5a). We calculated the ED50 (Effective Dose 50%) for each combination of serum
294 and virus. The ED50 were high for D614G (ED50 of $6.7x10^3$) and were decreased by 5-fold for BA.1 and
295 BA.5, confirming the escape properties of these previous sublineages [36]. With the XBB-derived strains,
296 the ED50 were low, ranging from $2x10^2$ to $8x10^1$. XBB.1.16.1 and EG.5.1.3 neutralization titers were
297 the lowest (22 and 30-fold lower than BA.1, respectively). BA.2.86.1 neutralization was about 2-fold
298 more sensitive to neutralization than EG.5.1.3, confirming recent results [16,21-30].

299 We then asked how a boost with the bivalent original/BA.5 Pfizer mRNA vaccine modified
300 these humoral responses. Sera from 20 and 15 individuals were tested one month and six months
301 (Tables S2b,c) after the bivalent boost, respectively (Fig. 6b-c). After one month, titers were increased
302 against all tested variants, when compared to individuals that did not receive the boost (Fig. 6a,b). The
303 highest responses were detected against D614G, and to a lower extent to BA.1 and BA.5, reflecting a
304 probable imprinting of the immune response. The responses against the recent XBB-derived and
305 BA.2.86 variants remained about 10-25 fold lower than against BA.5. A similar trend was observed six
306 months after the boost. Neutralization was reduced against all strains, highlighting the declining
307 humoral response [54,55]. The neutralizing activity was barely detectable against XBB.1.16.1, EG.5.1.3 and
308 BA.2.86.1 (Fig. 6c). We confirmed the stimulation and subsequent decline of the response elicited by
309 the boost by longitudinally analyzing 15 individuals, tested before and one, three and six months after
310 vaccine administration. The neutralizing titers peaked at one month and then progressively declined
311 over time (Fig. 6d). The decreases of neutralization titers for all variants, compared to D614G, in the
312 various categories of sera, are depicted Table S4.

313 Altogether, these results indicate that the XBB-derived and BA.2.86.1 variants are poorly
314 neutralized by sera from individuals having received 3 doses of the original monovalent vaccine. A
315 bivalent boost increased neutralizing titers, which remained however low with EG.5.1.3, XBB.1.16.1
316 and BA.2.86.1.

317

318

319

320 **Impact of XBB breakthrough infections on neutralization.**

321 We then examined the impact of breakthrough infections on the cross-neutralizing activity of
322 serum antibodies. We analyzed the sera from twelve individuals that were infected in September 2023
323 (Table S2d), at a time where the main variants circulating in France were XBB.1.9*, XBB.2.3* and
324 XBB.1.16* (representing 49%, 20%, and 14% of the sequenced cases respectively) (GISAID
325 https://www.epicov.org). Samples were analyzed about 3 weeks post-infection (median 19 days; range
326 10-50 days). A strong augmentation of neutralization against all viruses tested was observed, with
327 ED50 between $1.5x10^3$ to $1.4x10^4$ (Fig. 6e). Compared to BA.1, the Nab titers were reduced by about
328 4-fold against EG.5.1.3 and BA.2.86.1 (ED50 of $2x10^3$, respectively). Therefore, post-vaccination
329 breakthrough infection during circulation of XBB-related viruses led to an increase in neutralizing
330 antibody titers, with reduced disparities between variants. This suggests that the anamnestic humoral
331 response triggered by XBB infection includes both a recall of a B-cell memory and the induction of a
332 cross-neutralizing immunity.

333

334 **Comparison of BA.2.86.1 and JN.1 variants.**

335 BA.2.86 worldwide circulation has been associated with a rapid diversification. Multiple
336 sublineages, some carrying substitutions in the spike, have been designated (Fig. 7a). As mentioned
337 above, the JN.1 sublineage became predominant worldwide in December 2023-Januray 2024. We thus
338 compared BA.2.86.1 and JN.1 fusogenicity, affinity to ACE2, replication in hNECs and sensitivity to
339 immune sera (Fig. 7). The fusogenic potential of BA.2.86.1 and JN.1 was globally similar, as assessed
340 by visualizing the syncytia formed upon infection of S-Fuse cells (Fig. 7b). The affinity to ACE2 was
341 measured as described above. The EC50 of ACE2 binding was enhanced by 1.8-fold for JN.1, indicating
342 a decreased affinity for the receptor (Fig. 7c). In hNECs, both variants replicated with no significant
343 differences observed at 24 hours p.i. (Fig. 7d). The sensitivity of JN.1 to neutralization by sera from
344 individuals having received three doses of the original Pfizer vaccine was particularly low, with about
345 a 2-fold decrease in EC50 compared to BA.2.86.1 (Fig. 7e and Table S4). A similar trend was observed
346 after a BA.5 bivalent vaccine boost, which triggered a moderate and short-lasting increase in NAb levels
347 (Fig. 7e). However, a breakthrough XBB infection enhanced neutralization titers to ED50 about 10^3,
348 with no significant differences between BA.2.86.1 and JN.1 (Fig. 7e). Therefore, as described above
349 with other recently circulating XBB-derived variants, an XBB breakthrough infection triggered a cross-
350 protective response allowing a moderate but significant neutralization of JN.1 (Fig. 7e and Table S4).

351 Thus, JN.1 displays lower affinity to ACE2 and higher immune evasion properties compared to
352 BA.2.86.1, which likely contributes to its success, possibly in combination with epidemiological factors.

353

354

355 **Discussion**

356 We show that the predominant SARS-CoV-2 Omicron variants circulating in the fall 2023 have
357 progressed towards both increased fitness, as visible in primary cell cultures, and enhanced immune
358 evasion properties. Independently, a novel variant has emerged, similarly presenting high fitness and
359 immune evasion despite a distinct constellation of changes. The tropism of the recent variants for cell
360 lines has also changed. Vero E6 cells no longer allowed efficient replication of EG.5.1.1,
361 EG.5.1.3,BA.2.86.1 and JN.1 strains. Addition of TMPRSS2 did not necessarily increase replication of
362 these recent strains in Vero E6 cells, as illustrated by the discrepant results obtained with Vero E6 TMP-
363 1 and TMP-2 clones. Clonal specificities may explain these differences. However, efficient viral
364 replication occurred in Vero E6 TMP-2 cells, that express low levels of TMPRSS2, and not in Vero E6
365 TMP-1, that express high levels of TMPRSS2. This protease primes the spike for fusion, but also cleaves
366 ACE2 [37]. Initial SARS-CoV-2 variants used both cleaved and uncleaved ACE2 as a receptor, whereas a
367 shift towards preferential use of uncleaved ACE2 for Omicron variants has been proposed [56]. Our
368 results strongly suggest that a delicate balance between ACE2 and TMPRSS2 levels is necessary for
369 optimal replication of recent variants in Vero E6 cells.

370 We previously reported that IGROV-1 cells are highly permissive to previous SARS-CoV-2
371 strains[36]. We extend here this observation to XBB-derived and BA.2.86.1/JN.1 strains and explore the
372 underlying mechanisms. Another study confirmed the sensitivity of IGROV-1 cells to SARS-CoV-2 and
373 reported that the cells are not defective in their interferon response to infection [57]. We show that
374 IGROV-1 cells naturally express ACE2 but are negative for TMPRSS2, using a sensitive anti-TMPRSS2
375 nanobody [58]. Moreover, the TMPRSS2 inhibitor Camostat did not impair infection in IGROV-1 but was
376 active in Vero E6 TMP-1 cells, confirming the absence of TMPRSS2 in IGROV-1 cells. In contrast, two
377 cathepsin inhibitors, SB412515 and E-64d strongly inhibited viral infection in IGROV-1, but acted poorly
378 in Vero E6 cells and were inefficient in Vero E6 TMP-1 cells. Our results indicate that the high
379 permissibility of IGROV-1 to all SARS-CoV-2 strains is likely due to an efficient TMPRSS2-independent
380 endocytic viral entry pathway.

381 We studied the fusogenicity and receptor binding properties of the variant spikes. The EG.5.1,
382 BA.2.86.1 and JN.1 spikes were not more fusogenic than BA.1 and BA.4/5 spikes, and even less than
383 BQ.1.1 and XBB.1.5. The selective advantage of the most recent variants is thus not associated to an
384 increased ability to fuse and to form syncytia, at least in the cell lines tested. Addition of TMPRSS2 in
385 target cells similarly increased fusion with the different spikes, indicating that they remain sensitive to
386 the protease. The BA.2.86.1 spike expressed at the surface of infected cells bound with higher affinity
387 to ACE2 than EG.5.1.3 and XBB.1.16.1 (3.5-fold and 4.3-fold decrease in EC50, respectively). This
388 confirms recent results obtained with recombinant proteins and might be linked to a better exposure
389 of the BA.2.86 RBD than those of XBB-derived or EG.5.1 strains [28]. This increased affinity may

390 contribute to immune escape by itself. In addition, variants with high affinity for ACE2 may have a
391 stronger evolutionary potential as they could tolerate more escape mutations in the RBD despite their
392 negative impact on ACE2 binding, as seen for instance with JN.1.

393 XBB.1-derived variants, BA.2.86.1 and JN.1 rapidly and potently replicated in primary nasal
394 epithelial cells, amplifying a trend already observed with previous Omicron variants [40,59]. This efficient
395 replication was previously associated with a greater dependency of Omicron on endocytic entry and a
396 lower usage of TMPRSS2 in these cells [40,59], although this last point remains debated [41]. We show here
397 that as soon as 24 h pi, vRNA release of recent variants was up to 380-fold higher than Delta, and 6-
398 fold higher than BA.1. Among the recent variants, EG.5.1.3 was the fittest and fastest. The cytopathic
399 effect was particularly marked with EG.5.1.3 and BA.2.86.1. Infection with these two variants was
400 associated with a strong disappearance of cilia, a phenomenon described with other strains [47], and
401 with caspase activation. This accelerated replication in respiratory cells likely represents an important
402 factor explaining the selective advantage and improved transmissibility of the variants. Future work
403 will help determining how ACE2 affinity, entry pathways, TMPRSS2 usage, likely involving distinct
404 combinations of changes in XBB and BA.2.86, as well as mutations in other proteins are regulating viral
405 fitness in this relevant in vitro model.

406 The antiviral drugs Paxlovid, Remdesivir and Molnupiravir remain active against XBB-derived and
407 BA.2.86 variants, indicating that this therapeutic arsenal is so far not impacted. However, there is no
408 approved mAb remaining on the market. Sotrovimab, which retained partial antiviral activity against
409 BQ.1.1 and XBB.1.5 [50], poorly acted on EG.5.1.3 and no longer binds or inhibits BA.2.86.1 and JN.1. This
410 novel lineage carries numerous mutations known to allow mAb evasion [28], including the K356T
411 substitution conferring resistance to Sotrovimab [51] [52]. Novel mAbs are under pre-clinical and clinical
412 development [11,60,61]. It will be worth scrutinizing their antiviral activity against BA.2.86.1/JN.1 and other
413 emerging subvariants.

414 Sera from individuals who had received three doses of COVID-19 Pfizer BNT162b2 vaccine
415 displayed almost no neutralization activity against the recent XBB-derived or BA.2.86 variants. Bivalent
416 boosters increased neutralization titers but only for an abbreviated period of time. Six months after
417 the boost, the efficacy of the sera against EG.5.1.3 and BA.2.86.1/JN.1 was barely detectable. This
418 confirms reports indicating that these two variants are among the most immune evasive viruses
419 described so far, even if some variations between studies have been observed [16,21-30].

420 We further show that breakthrough infections that occurred in September 2023, during XBB
421 circulation, triggered a broader cross-neutralizing response than bivalent boosters. The differences
422 between variants were reduced, XBB.1, EG.5.1 and BA.2.86.1 neutralization was globally similar in
423 individuals who experienced such XBB breakthrough infections. Therefore, in addition to imprinted
424 memory, other mechanisms linked to hybrid immunity, such as the generation of responses targeting

425 novel antigens can be efficacious. This observation is in line with reports indicating that XBB.1.5-
426 containing monovalent mRNA vaccines elicit cross-reactive immune responses targeting EG.5.1 and
427 BA.2.86 variants [62,63]. Neutralization titers were however lower against all XBB-derived and BA.2.86
428 variants than against BA.4/5 [62,63]. There is a debate about the interest of annually administrating
429 vaccines based on the circulating variants, especially in healthy individuals [64]. It will be important to
430 analyze the longevity of the humoral response generated by the recent XBB.1.5-based vaccines, and
431 its link with the duration of clinical efficacy against severe forms of the disease.

432 We also isolated and analyzed the properties of JN.1, a BA.2.86.1 sublineage carrying the L455S
433 spike substitution, that rapidly expanded worldwide and. JN.1 displays noticeable differences relative
434 to BA.2.86.1. Its affinity to ACE2 is decreased and its immune evasion properties are higher. We did
435 not detect major differences in the replication of BA.2.86.1 and JN.1 in primary hNECs. Future work
436 will help understand whether the high transmissibility of JN.1 in humans is only due to immune evasion
437 or also associated with other viral properties.

438 There are limitations to our study. Firstly, we analyzed a limited number of serum samples.
439 However, the marked differences between variants and groups of individuals allowed statistical
440 analysis. Secondly, this work did not include other emerging XBB sublineages showing further evidence
441 of convergent evolution and increasing in frequency. Multiple lineages (e.g. GK.1.1 or JD.1.1 from
442 XBB.1.5; HK.3 or JG.3 from XBB.1.9.2; JF.1 from XBB.1.16; or DV.7.1 from BA.2.75) have independently
443 acquired the F455L substitution in addition to F486P and F456L, a change parallel to the L455S
444 substitution noted in JN.1. Thirdly, we did not explore the role of individual mutations within the spike
445 or in other viral proteins known to have changed in Omicron variants [65]. Fourthly, the method
446 employed here to assess the affinity of various variants for ACE2 is less precise than Bio-Layer
447 Interferometry (BLI), which requires the use of recombinant soluble proteins. However, our approach
448 offers the advantage of assessing the conformation of the Spike protein on the surface of infected
449 cells. Our results are however consistent with recent reports [29] [28]. Further research to investigate the
450 mechanisms associated with the modifications of viral properties described here will be relevant in
451 understanding the processes underlying the evolution of SARS-CoV-2.

452 In summary, we show that SARS-CoV-2 Omicron variants continuously evolve in a context of the
453 mixed immunity of human populations. The selective advantage of EG.5.1 and BA.2.86.1/JN.1 variants
454 combines both convergent increased fitness and replication in respiratory cells, and resistance to the
455 most prevalent antibodies.

456 **Materials & Methods**

457 Our research fulfills all relevant ethical requirements. An informed consent was obtained from all
458 participants. No statistical methods were used to predetermine sample size and the experiments were
459 not randomized. The investigators were not blinded. Sex or gender analysis was not performed due to
460 the limited number of participants.

461

462 **Cohorts**

463

464 **Serum from bivalent Wuhan/BA.5 Pfizer vaccine recipients or from infected individuals (Orléans,**
465 **France).**

466 The Neutralizing Power of Anti-SARS-CoV-2 Serum Antibodies (PNAS) cohort is an ongoing
467 prospective, monocentric, longitudinal, observational cohort clinical study aiming to describe the
468 kinetics of neutralizing antibodies after SARS-CoV-2 infection or vaccination (ClinicalTrials.gov
469 identifier: NCT05315583). The cohort takes place in Orléans, France and was previously described [66].
470 This study was approved by the Est II (Besancon) ethical committee. At enrollment, written informed
471 consent was collected, and participants completed a questionnaire that covered sociodemographic
472 characteristics, clinical information and data related to anti-SARS-CoV-2 vaccination.

473

474 **Serum from bivalent Wuhan/BA.5 Pfizer vaccinated individuals from Lyon, France.**

475 A prospective, multicentric, longitudinal, interventional cohort clinical study (COVID-SER) is
476 conducted at Hospices Civils de Lyon with the objective to evaluate the effectiveness of commercially
477 developed serological test kits currently in development, which will be used for the diagnosis of
478 patients with suspected SARS-CoV-2 infection. The COVID-SER-VAC ancillary study where blood
479 samples was collected at the time of the injection(s) as per the recommended vaccination schedule
480 was conducted (ClinicalTrials.gov identifier: NCT04341142) [67]. A sub-study aimed to build a collection
481 of biological samples and transfer of residual blood products to external partners for the advancement
482 of scientific knowledge on SARS-CoV-2. We had access to 23 serum samples from hospital staff who
483 were vaccinated with the bivalent Pfizer vaccine. Samples were taken at the time of the injection, 1
484 month, and 6 months after the injection At enrollment, written informed consent was collected.
485 Virological findings (SARS-CoV-2 RT–qPCR results, date of positive test, screening, or sequences results)
486 and data related to SARS-CoV-2 vaccination (brand product, date of first, second, third and fourth
487 vaccination) were also collected.

488

489 **Virus strains**

490 The D614G, Delta, BA.1, BA.5 and BQ.1.1 and XBB.1.5 strains have been described [36,50,68,69].

491 The XBB.1 strain (hCoV-19/France/PAC-HCL022171892001/2022) strain was supplied by the
492 National Reference Centre for Respiratory Viruses hosted by the Hôpital de la Croix-Rousse (Lyon,
493 France) and headed by Dr Bruno Lina.

494 The XBB.1.9.1 strain (hCoV-19/France/GES-IPP08594/2023) was supplied by the National
495 Reference Centre for Respiratory Viruses hosted by Institut Pasteur (Paris, France). The human sample

496 from which strain hCoV-19/France/GES-IPP08594/2023 was isolated, was provided by Dr Djoubi from
497 Massif des Vosges Hospital (France).
498 The XBB.1.16.1 strain (hCoV-19/France/GES-IPP07712/2023) was supplied by the National
499 Reference Centre for Respiratory Viruses hosted by Institut Pasteur. The human sample was provided
500 by Dr Vanessa Cocquerelle from Laboratory Deux Rives (France).
501 The XBF strain (hCoV-19/France/IDF-APHP-HEGP-81-10-2332993394/2023) was isolated from a
502 nasopharyngeal swab of individuals attending the emergency room of Hôpital Européen Georges
503 Pompidou (HEGP); Assistance Publique, Hôpitaux de Paris.
504 The EG.5.1.1 strain (hCoV-19/France/GES-IPP15954/2023) was supplied by the National
505 Reference Centre for Respiratory Viruses hosted by Institut Pasteur. (The human sample was provided
506 by Dr Valérie Herzig from Laboratoire Lenys, Colmar (France).
507 The EG.5.1.3 strain (hCoV-19/France/BRE-IPP15906/2023) was supplied by the National
508 Reference Centre for Respiratory Viruses hosted by Institut Pasteur (Paris, France) The human sample
509 was provided by Dr F. Kerdavid from Laboratoire Alliance Anabio, Melesse (France).
510 The BA.2.86.1 strain (hCoV-19/France/IDF-IPP17625/2023) was supplied by the National
511 Reference Centre for Respiratory Viruses hosted by Institut Pasteur. The human sample was provided
512 by Dr Aude Lesenne from Cerballiance, Lisses (France).
513 The JN.1 strain (hCoV-19/France/HDF-IPP21391/2023) was supplied by the National Reference
514 Centre for Respiratory Viruses hosted by Institut Pasteur. The human sample was provided by Dr Bruno
515 Foucault from Laboratoire Synlab Normandie Maine, La Ferté Macé (France).
516 All patients provided informed consent for the use of their biological materials. Viral strains were
517 amplified through one or two passages on Vero E6, Vero E6 TMPRSS2, or IGROV-1 cells. Supernatants
518 were harvested two or three days after viral exposure. The titration of viral stocks was performed on
519 S-Fuse cells [36,42]. Viral supernatants were sequenced directly from nasopharyngeal swabs and after
520 isolation and amplification on Vero E6 or IGROV-1 cells.
521 For sequencing, an untargeted metagenomic sequencing approach was used, including
522 ribosomal RNA (rRNA) depletion. In brief, RNA was extracted using the QIAamp Viral RNA extraction
523 kit (Qiagen) with the provided poly-A RNA carrier. Prior to library construction, carrier RNA and host
524 rRNA were depleted using oligo(dT) and custom probes, respectively. The resulting RNA from selective
525 depletion was utilized for random-primed cDNA synthesis with SuperScript IV RT (Invitrogen). Second-
526 strand cDNA was generated using Escherichia coli DNA ligase, RNase H, and DNA polymerase (New
527 England Biolabs), and then purified with Agencourt AMPure XP beads (Beckman Coulter). Libraries
528 were prepared using the Nextera XT kit and sequenced on an Illumina NextSeq500 platform (2 × 75
529 cycles). Reads were assembled using Megahit v1.2.9. The sequences have been deposited on the
530 GISAID EpiCoV database (Table S3).

531 **Cell lines**

532 IGROV-1, Vero E6 and Vero E6 TMPRSS2 clone 1 (Vero E6 TMP-1) and S-Fuse cells were described
533 previously [42 36]. Vero E6 TMP-2 cells were kindly provided by Dr Makoto Takeda lab [38]. 293T (CRL-3216)
534 and U2OS (Cat# HTB-96) cells were obtained from ATCC. Cells regularly tested negative for
535 mycoplasma.

536 **Infection of IGROV-1, Vero E6, Vero E6 TMP-1 and Vero E6 TMP-2 cells**

537 Six hours before infection, 30,000 cells were seeded in a µClear black 96-well plate (Greiner Bio-
538 One). Cells were then infected with the indicated strains of SARS-CoV-2, as described in legend of
539 Figures 2 and S3 (specifying the variants and quantities of virus used). At days 1 to 4 post-exposure,
540 the cells were fixed using 4% PFA (Electron microscopy cat# 15714-S). The cells were then
541 intracellularly stained with anti-SARS-CoV-2 nucleoprotein (N) antibody NCP-1 (0.1 µg/mL) as
542 described [36]. This staining was carried out in PBS with 0.05% saponin 1% BSA, and 0.05% sodium azide
543 for 1 h. the cells were washed twice with PBS and stained with anti-IgG Alexa Fluor 488 (dilution 1:500,
544 Invitrogen; cat# A11029) for 30 minutes before being washed twice with PBS. Hoechst 33342
545 (Invitrogen, cat# H3570) was added during the final PBS wash. Images were captured using an Opera
546 Phenix high-content confocal microscope (PerkinElmer). The N-positive area and the number of nuclei
547 were quantified using Harmony Software v4.9 (PerkinElmer).
548

549 **Test of Antiviral molecules.**

550 Cells were seeded in a µClear black 96-well plate (Greiner Bio-One) and pretreated for 2 hours
551 with Camostat (Sigma, cat# E8640), E-64d (Sigma, cat# SML0057), SB412515 (Cayman Chemical, cat#
552 23249), Nirmatrelvir (MedChemExpress; cat# HY-138687), Remdesivir (MedChemExpress; cat# HY-
553 104077), or Molnupinavir (MedChemExpress; cat# HY-135853) at concentrations as described in the
554 figure legends. Cells were infected with the indicated SARS-CoV-2 strains. After 24h, infection was
555 revealed as described above. The percentage of inhibition of infection was calculated using the area
556 of N-positive cells as a value with the following formula: 100 × (1 − (value with drugs − value in 'non-
557 infected')/(value in 'no drugs' − value in 'non-infected')).

558 The monoclonal antibodies used in this study were previously described [36,69]. Neutralizing
559 activity and ED50 were measured as described in the "S-Fuse neutralization assay" section.
560

561 **Plasmids**

562 SARS-CoV-2 spikes (from D614G, Delta, BA.1, BA.4/5, BQ1.1, XBB.1.5/9, XBB.1.16, EG.5.1, BA.2.86
563 isolated) were human codon-optimized and produced in silico (GeneArt, Thermo Fisher Scientific) as
564 described [42,44]. Spike sequences were cloned into a phCMV backbone (GenBank: AJ318514) using

565 Gateway cloning (Thermo Fisher Scientific) or restriction enzyme digestion followed by ligation with
566 T4 DNA ligase (New England Biolabs). The pQCXIP-Empty plasmid was used as a negative control [42,44].
567 All plasmids were sequenced by the Eurofins Genomics TubeSeq service. His-tagged recombinant ACE2
568 ectodomain (amino acids 19–615) was cloned into pcDNA3.1 vector, produced by transient
569 transfection of HEK293-F cells, and purified by affinity chromatography. Purified ACE2 protein was
570 biotinylated using the EZ-Link Sulfo-NHS-Biotin kit (Thermo Fisher Scientific) as reported previously [70].
571
572 **Donor Acceptor fusion assay**
573 To assess the fusion of the respective spike constructs, syncytia formation assays were
574 performed as described [42,44]. Briefly, 293T-GFP-11 cells were transfected in suspension at 37°C for 30
575 minutes. The transfection mix was prepared using Lipofectamine 2000 (Thermo Fisher, Scientific 179)
576 with 50 ng of DNA in a 1:10 ratio of SARS-CoV-2-S and pQCXIP-Empty, respectively, before being added
577 to the cells. Following transfection, cells were washed and resuspended in DMEM with 10% FBS. The
578 level of transfection was quantified by surface staining of Spike with pan-coronavirus mAb10
579 antibody[36] 18 h post-transfection. Subsequently, 30,000 transfected HEK293T cells were co-cultured
580 with 15,000 IGROV-1-GFP-1-10, VeroE6-GFP1-10, or VeroE6 TMP-1 GFP-1-10 cells per well in a µClear
581 black 96-well plate. 18 h post-transfection, Hoechst 33342 (Invitrogen, cat# H3570) was added to the
582 media at a 1:10,000 dilution and images were acquired using the Opera Phenix High-Content Screening
583 System (PerkinElmer). Analysis was performed using Harmony 191 High-Content Imaging and Analysis
584 Software (PerkinElmer, HH17000012, v.5.0), including the counting of nuclei and the GFP area.
585
586 **Soluble ACE2 binding**
587 IGROV-1 cells were seeded in a 6-well plate 12 h before infection with the indicated SARS-CoV-
588 2 variants. The viral inoculum amount was calculated to achieve 50% of infected cells (N-positive cells)
589 at 24 h post-infection. Afterward, the cells were detached in PBS-EDTA (0.1%) and split into a 96-well
590 plate, with 200,000 cells per well. Cells were incubated with serial dilutions concentrations of a soluble
591 biotinylated human ACE2 [70]. Cells were washed twice with PBS and stained with Streptavidin Alexa
592 Fluor 647 (dilution 1:500, Invitrogen; cat# S32357) for 30 minutes. Cells were then washed twice with
593 PBS and fixed using 4% PFA (Electron microscopy; cat# 15714-S). Cells were then intracellularly stained
594 with anti-SARS-CoV-2 nucleoprotein (N) antibody NCP-1, as described above. Cells were acquired using
595 an Attune NxT Flow Cytometer (Thermo Fisher). Data were analyzed using FlowJo software
596 (BDBioSciences).
597
598
599

600 **S-Fuse neutralization assay**

601 U2OS-ACE2 GFP1-10 or GFP 11 cells, also termed S-Fuse cells, become GFP+ when they are
602 productively infected by SARS-CoV-2 [42 71]. Cells were mixed (ratio 1:1) and plated at 8×10^3 per well in
603 a µClear 96-well plate (Greiner Bio-One). The indicated SARS-CoV-2 strains were incubated with serially
604 diluted monoclonal antibodies or sera for 15 min at room temperature and added to S-Fuse cells. Sera
605 were heat-inactivated for 30 min at 56 °C before use. 18 h later, cells were fixed with 2% PFA (Electron
606 microscopy cat# 15714-S), washed and stained with Hoechst (dilution of 1:1,000, Invitrogen, Invitrogen
607 cat# H3570). Images were acquired using an Opera Phenix high-content confocal microscope
608 (PerkinElmer). The GFP area and the number of nuclei were quantified using the Harmony software
609 (PerkinElmer). The percentage of neutralization was calculated using the number of syncytia as value
610 with the following formula: 100 × (1 – (value with serum – value in 'non-
611 infected')/(value in 'no serum' – value in 'non-infected')). Neutralizing activity of each serum was
612 expressed as the half maximal effective dilution (ED50). ED50 values (in ng/ml for monoclonal
613 antibodies and in dilution values – i.e titers – for sera) were calculated with a reconstructed curve using
614 the percentage of neutralization at each concentration.

615

616 **Human nasal epithelium cells (hNEC) culture, infection and imaging**

617 MucilAirTM, reconstructed human nasal epithelial cells (hNECs) that had been differentiated for
618 4 weeks prior to obtention, were cultured in 700 µl MucilAirTM media on the basal side of the air/liquid
619 interface (ALI) cultures and monitored for healthy cilia movements. One hour prior to infection, mucus
620 was removed from the apical side of the culture by washing the apical side with warm 200 µl MucilAir™
621 media. Cells were then infected with equal virus titres in 100 µL MucilAir™ media for 2 hours. Viral
622 input was removed and stored at -80°C. Cells were then washed 2 times for 10 min at 37°C in warm
623 PBS and then 20 min in 200 µL MucilAir™ media for the day 0 recording. Washing with 100 µl of
624 MucilAir™ warm media was repeated every 24 h for 96 h. Every wash was subsequently centrifuged
625 at 1500 rpm to remove cell debris and frozen at -80°C. After 96 h, cells were fixed on the apical and
626 basal sides with 4% PFA for 45 minutes. For imaging, fixed cells were stained intracellularly with anti-
627 SARS-CoV-2 nucleoprotein (N) antibody NCP-1, anti-alpha tubulin (66031-1-Ig; Proteintech), rabbit
628 anti-cleaved caspase-3 (D175; Cell Signaling Technology) and phalloidin-Atto 565/633 (75784-1MG-F;
629 Sigma) and imaged using the LSM-700 confocal microscope (Zeiss) as described [58 44].

630

631 **Staining of ACE2 and TMPRSS2**

632 Surface expression of TMPRSS2 and ACE2 was assessed on live cells by staining with anti-
633 TMPRSS2 VHH-A01-Fc [58] at 1 µg/ml or with anti-ACE2 VHH-B07-Fc (Brelot et al, manuscript in
634 preparation) at 0.5 µg/ml, for 30 min at 4°C in MACS buffer. Then, cells were stained with Alexa Fluor

635 647-conjugated goat anti-human antibody (Invitrogen; cat# A-21445, 1/500). The control VHH Fc
636 (R3VQFc) recognizes an unrelated protein (phosphorylated Tau protein).
637
638 **Phylogenetic tree inference and lineage monitoring**
639 All available SARS-CoV-2 sequences from human infections were downloaded from the GISAID
640 Epicov database (https://gisaid.org/) on November 27, 2023, and only sequences longer than 29000
641 nucleotides and with less than 1% ambiguities (Ns) were kept. SARS-CoV-2 contextual sequence names
642 were retrieved from the Nextstrain build of Sept. 18, 2023 [72]. Sequences were reannotated using
643 pangolin (v4.3.1, with option --usher), and aligned against the Wuhan-Hu1 reference sequence
644 (GenBank MN908947) using nextalign v2.14.0. In addition to this global context, BA.2.86 sequences
645 were added to the dataset, using gofasta v1.2.1 [73]. The alignment used for phylogenetic reconstruction
646 was made of 2909 sequences (global context sequences with the addition of BA.2.86 sequences and
647 their closest relatives). Specific positions of the alignment were masked using goalign v0.3.5 (goalign
648 mask command) to decrease phylogenetic noise. Bootstrap alignments were generated using goalign
649 v0.3.5 (goalign build seqboot command) and reference and bootstrap trees were inferred using iqtree
650 v2.2.0 (iqtree -m GTR -ninit 2 -n 2 -me 0.05 -nt AUTO -ninit 10 -n 4). Bootstrap supports were computed
651 using gotree v0.4.4 (gotree compute support fbp).
652 Mutations that are common and specific to lineages of interest were computed using the
653 outbreak.info R package (https://outbreak-info.github.io/R-outbreak-info) on January 16, 2023. Values
654 for some insertions or deletions were manually computed. Hierarchical relationships between lineages
655 were retrieved from the pangolin GitHub repository (https://github.com/cov-lineages/pango-
656 designation).
657 The evolution of the prevalence of SARS-CoV-2 lineages throughout 2023 was visualized using
658 R 4.3 and ggplot 3.4.3, using GISAID data from January 1 to December 31, 2023. Data and workflows
659 used to generate the figures are publicly available at
660 https://github.com/SimonLoriereLab/sarscov2_Oct2023.
661 All genome sequences and associated metadata used to build Fig. 1 and S1 are published in
662 GISAID's EpiCoV database. To view the contributors of each individual sequence with details such as
663 accession number, Virus name, Collection date, Originating Lab and Submitting Lab and the list of
664 Authors, visit https://doi.org/10.55876/gis8.240122bu (Fig. 1a) or
665 https://doi.org/10.55876/gis8.231020kn (Fig. 1b).
666
667 **Statistical analysis**
668 Flow cytometry data were analysed using FlowJo v.10 (TriStar). Calculations were performed
669 using Excel 365 (Microsoft). Figures were generated using Prism 9 (GraphPad Software). Statistical

670 analysis was conducted using GraphPad Prism 9. Statistical significance between different groups was
671 calculated using the tests indicated in each figure legend.
672
673 **Data availability**
674 All data supporting the findings of this study are available within the article or from the corresponding
675 authors upon reasonable request without any restrictions. The raw data generated in this study are
676 provided in the Source Data file. The sequencing data generated in this study have been deposited in
677 the GISAID EpiCoV database (EPI_SET ID: EPI_SET_231113yq).
678
679
680 **Figure Legends.**
681
682 **Figure 1. SARS-CoV2 evolution in 2023 and Spike mutation patterns of the main lineages. a.** Evolution
683 of the prevalence of main SARS-CoV-2 lineages from January to **December 31**, 2023. The pattern of
684 emergence and replacement of several lineages, such as XBB.1.5, then XBB.1.9, XBB.1.16 or EG.5.1 and
685 the emergence of BA.2.86 and JN.1 is shown. The variants with a frame are analyzed in this study. **b.**
686 Changes specific to lineages studied here in comparison to BA.2 are displayed as colored squares. The
687 spike domain organization is displayed on the top, with N-terminal domain (NTD), Receptor Binding
688 Domain (RBD), Receptor Binding Motif (RBM), Single domains SD1 and SD2, S1/S2 cleavage site, and
689 S2 domains. BA.2.86 and its descendant JN.1 show many new mutations compared to other lineages.
690 A complete comparison of spike mutations compared to the reference Wuhan_Hu-1 is presented in
691 Fig. S1b.
692
693 **Figure 2. Replication kinetics of SARS-CoV-2 variants in Vero E6, Vero E6 TMP-1 and -2 and IGROV-1**
694 **cells. a.** Cells were infected with the indicated variants, at 3x10-2 infectious units per cell. Cells were
695 stained with a pan-coronavirus anti-N antibody at days 1 to 4 pi. The N-positive areas were plotted on
696 the graph. Each curve represents an independent experiment. **b.** Comparison of the effect of E-64d
697 and SB412515 against different variants. IGROV-1 cells were pre-incubated 2 h with serial dilutions of
698 E-64d or SB412515 (30 to 1.7x10-4 µM) and infected with D614G, XBB.1.5, EG.5.1.3, or BA.2.86.1. The
699 percentage of inhibition is represented. Data are mean ± s.d. of 3 independent experiments.
700
701 **Figure 3. Fusogenicity and binding to ACE2 of the variant spike proteins. a.** Schematic representation
702 of the coculture system. 293T GFP-11 donor cells were transfected with the indicated variant spike
703 expression plasmids and cocultivated with IGROV-1, Vero E6 or Vero E6 TMP-1 acceptor cells
704 expressing GFP1-10. The area of GFP+ fused cells was measured after 18 h. **b.** Representative images

705 of cell-cell fusion between 293T donor cells and IGROV-1 acceptor cells. Scale bar, 200 µm. **c.**
706 Fusogenicity of the different spikes with IGROV-1 acceptor cells. Each dot represents a single
707 experiment. Data are mean ± s.d. of 4-6 independent experiments. One-way ANOVA with Kruskal-
708 Wallis test followed by Dunn's test for multiple comparisons to compare Delta with respective variants
709 were conducted. **d.** Effect of TMPRSS2 on the fusion of the different spikes. Cell-cell fusion assays were
710 performed with Vero E6 or Vero E6 TMP-1 as target cells. Data are mean ± s.d. of 4 independent
711 experiments. Paired t-test to compare fusion in Vero E6 versus Vero E6 TMP-1 were conducted. **e,f.**
712 Binding of soluble ACE2 to IGROV-1 infected cells (e) or to 293T cells transiently expressing the Spike
713 (f). Cells were stained with serial dilutions of soluble ACE2. The EC50 of ACE2 binding (µg/ml) for the
714 indicated spike proteins is shown. Data are mean ± s.d. of 3-4 independent experiments. One-way
715 ANOVA with Kruskal-Wallis test followed by Dunn's test for multiple comparisons to compare Delta
716 with respective variants were conducted.
717
718 **Figure 4. Replication of SARS-CoV-2 variants in hNECs.** Primary human nasal epithelial cells (hNECs)
719 cultivated at the air-liquid interface (ALI) were exposed to the indicated SARS-CoV-2 variants. **a.** Viral
720 RNA release from the apical side of hNECs was measured by RT-qPCR every day up to 4 days p.i..
721 Replication kinetics of each variant from one representative experiment are represented. **b.**
722 Comparison of viral RNA release at day 1 pi with the indicated variants. **c.** Infectious viral titers in
723 supernatants from the apical side were quantified with S-Fuse cells at day 2 p.i. **b,c.** Data are mean ±
724 s.d. of 4-6 independent experiments. One-way ANOVA with Kruskal-Wallis test followed by Dunn's test
725 for multiple comparisons to compare Delta with respective variants were conducted. **d.**
726 Immunofluorescence of hNECs stained for tubulin (cyan), actin (yellow), SARS-CoV-2 Nucleocapsid
727 (green) and cleaved caspase-3 (red). Shown is one representative field (150x150 mm) of each variant.
728 Scale bar = 20 µm.
729
730 **Figure 5. Activity of neutralizing mAbs and antiviral drugs against SARS-CoV-2 variants. a.**
731 Neutralization curves of previously approved mAbs. Dose–response analysis of neutralization of the
732 indicated variants by Sotrovimab, Evusheld (Cilgavimab and Tixagevima) and Ronapreve (Casirivimab
733 and Imdevimab). **b.** Inhibitory curves of antiviral drugs against the indicated variants. Dose-response
734 analysis of the antiviral effect of Nirmatrelvir, Remdesivir and Molnupiravir. **a,b.** Data are mean ± s.d.
735 of 3 independent experiments.
736
737 **Figure 6. Sensitivity of SARS-CoV-2 variants to sera of vaccinated and/or infected individuals.**
738 Neutralization titers of the sera against the indicated viral variants are expressed as ED50. **a.**
739 Neutralizing activity of sera from individuals vaccinated with 3 doses of Pfizer vaccine. Sera (n= 21)

740 were sampled 25 – 475 days after the third dose. 13/21 had a breakthrough infection at the time of
741 BA.1/2 circulation. **b,c.** Neutralizing activity of sera from individuals having received the bivalent
742 Wuhan/BA.5 Pfizer boost. Sera were sampled one month (b; n= 20) and six months (c; n=14) after the
743 booster dose. **d.** Temporal evolution of Neutralizing Antibody (Nab) titers against D614G, BA.5,
744 EG.5.1.3 and BA.2.86.1 after bivalent Wuhan/BA.5 booster dose. The Nab titers were calculated at the
745 time of injection (month 0) and at the indicated months after injection. **e.** Neutralizing activity of sera
746 from Pfizer-vaccinated recipients after XBB-derived breakthrough infections (infections occurred in
747 September 2023, when XBB-derived variants were predominantly circulating in France). Sera were
748 sampled 10 to 50 days after the breakthrough (n=12). The dotted line indicates the limit of detection
749 (ED50 = 30). Each dot represents the mean of n=2 independent experiments. Black lines represent the
750 median values. Two-sided Friedman test with Dunn's test for multiple comparisons was performed to
751 compare each viral strain to D614G.
752
753 **Figure 7. Comparative analysis of BA.2.86.1 and JN.1 variants.**
754 **a.** Schematic tree describing BA.2.86 expanding diversity. Only substitutions in the spike are noted on
755 branches. **b.** Representative images of cell-cell fusion in S-Fuse cells after infection with BA.2.86.1 and
756 JN.1. Scale bar, 200 µm. **c.** Binding of soluble ACE2 to IGROV-1 infected cells. Infected cells were stained
757 with serial dilutions of soluble hACE2 (left panel). The EC50 of ACE2 (in µg/ml) is displayed (right panel).
758 Data are from two independent experiments in duplicate. **d.** Viral RNA release from the apical side of
759 hNECs was measured by RT-qPCR every day up to 4 days p.i.. Replication kinetics of BA.86.1 and JN.1
760 variants from one representative experiment out of 2 are represented (left). Comparison of viral RNA
761 release at day 1 pi with the indicated variants (right). **e.** Comparison of neutralization titers against
762 BA.2.86.1 and JN.1 in sera from individuals in the Orléans cohort. Neutralizing activity of sera (n=13)
763 from individuals vaccinated with 3 doses of Pfizer original vaccine, sampled 25-475 days after the third
764 dose (left panel). 9/13 had a breakthrough infection at the time of BA.1/2 circulation. Neutralization
765 activity of sera from recipients of a bivalent Wuhan/BA.5 booster dose. Sera were sampled at 1 (n=12),
766 3 (n=7) and 6 (n=8) months after the booster dose (middle panel). Neutralization activity of sera from
767 Pfizer-vaccinated individuals with a breakthrough infection in September 2023, when XBB-derived
768 variants were predominantly circulating in France (n=12) (right panel). Sera were sampled 10 to 50
769 days post-breakthrough infection. The dotted line indicates the limit of detection (ED50 = 30). Each
770 dot represents the mean of n=2 independent experiments. Black lines represent the median values.
771 c,d,e: Paired t-tests were conducted.
772
773 **Figure S1.** Maximum likelihood phylogeny representing the evolution of the main lineages of SARS-
774 CoV-2 since the beginning of the epidemic. **a.** The red circle indicates one of the first sequences

775 (Wuhan/Hu-1/2019). The BA.2.86 sequences are located inside the BA.2 clade, at the end of a long
776 branch. Of note, a limitation of the inferred phylogeny is that known recombinant lineages (e.g. XBF
777 or XBB) were included in the dataset, and their branching should be interpreted with caution. **b.**
778 Comparison of spike mutations compared to the reference Wuhan_Hu-1 for selected SARS-CoV-2
779 variants. The color scale reflects the frequency of the mutations within lineages based on the data
780 available on the GISAID EpiCoV database.
781
782 **Figure S2.** Additional mutations defining lineage JN.1 in comparison to its parent lineage BA.2.86.1.
783 The genome is drawn to scale, and for mutation leading to an amino acid change, the protein is
784 specified.
785
786 **Figure S3. ACE2 and TMPRSS2 expression in cell lines.** IGROV-1, Vero E6, Vero E6 TMP-1 and TMP-2
787 cells were stained with anti-ACE2 or anti-TMPRSS2 antibodies and analyzed by flow cytometry.
788 Representative examples of the gating strategy in IGROV-1 cells and of the signals obtained in cell lines
789 are shown.
790
791 **Figure S4. Permissibility of IGROV-1 and Vero E6 cells to SARS-CoV-2 variants.** Viral titrations in
792 IGROV-1 and Vero E6 cells. Cells were infected with serial dilutions of the indicated variants. At 24
793 hours post-infection (p.i.), cells were stained with a pan-coronavirus anti-N antibody (green) and
794 Hoechst to visualize the nuclei (blue). **a.** The N positive areas in IGROV-1 (blue curves) and Vero E6 cells
795 (grey curves) were compared for each viral dilution. The dotted line corresponds to the signal obtained
796 with the first dilution (1/20) in IGROV-1 cells, set to the arbitrary value of 1. Data are mean ± s.d. of 3-
797 5 independent experiments. **b.** Representative images with the indicated viral strains. An identical viral
798 inoculum was used in the two cell lines. Scale bar, 200 µm.
799
800 **Figure S5. Effect of the TMPRSS2 inhibitor Camostat and Cathepsin L inhibitors E-64d and SB412515**
801 **on viral infection a.** IGROV-1, Vero E6 and Vero E6 TMP-1 cells pre-incubated 2 h with Camostat (100
802 µM), E-64d (10 µM), or SB412515 (10 µM) and exposed to the D614G, Delta, BA.1, XBB.1, or XBB.1.16.1
803 variants for 24 h. The viral inoculum was determined by titration in each cell line to achieve a similar
804 N-positive area at 24 h pi. The cells were stained with a pan-coronavirus anti-N antibody. Hoechst was
805 used to visualize the nuclei for evaluating drug toxicity. The percentage of infection compared to the
806 control (without drugs, represented by the dotted line) is shown. Data are mean ± s.d. of 3 independent
807 experiments.
808

809 **Figure S6. Sensibility of BA.2.86.1 and JN.1 variants to TMPRSS2 inhibitor Camostat and Cathepsin L**
810 **inhibitors E-64d and SB412515.** IGROV-1 (a) and Vero E6 TMP-2 (b) cells pre-incubated 2 h with
811 Camostat (100 µM), E-64d (10 µM), or SB412515 (10 µM) and exposed to the Delta, BA.2.86.1 and JN.1
812 variants for 24 h. The viral inoculum was determined by titration in each cell line to achieve a similar
813 N-positive area at 24 h pi. The cells were stained with a pan-coronavirus anti-N antibody. Hoechst was
814 used to visualize the nuclei for evaluating drug toxicity. The percentage of infection compared to the
815 control (without drugs, represented by the dotted line) is shown. Data are mean ± s.d. of 2 independent
816 experiments.
817
818 **Figure S7. Spike expression in 293T cells.** Gating strategy and levels of Spike at the cell surface. 293T
819 cells transiently expressing the indicated variant Spikes were stained with a pan-coronavirus anti-S2
820 mAb 18 h post-transfection and analyzed by flow cytometry.
821
822 **Figure S8. Binding of variant Spike proteins to ACE2.** The affinity of the variant Spike proteins
823 expressed at the surface of IGROV-1 infected cells was assessed by staining the cells and flow
824 cytometry analysis. IGROV-1 cells were infected with the indicated variants. **a.** Representative
825 examples of the gating strategy. **b.** The percentages of biotinylated hACE2+ cells are represented at
826 various dilutions of hACE2-Fc. Data are mean ± s.d. of 3-4 independent experiments.
827
828 **Figure S9. Immunofluorescence of hNECs stained for cleavage products of caspase-3 and SARS-CoV-**
829 **2 nucleoprotein.** Quantification of total area of cleavaged caspase-3 and SARS-CoV-2 N. Each data
830 point represents one randomly assigned field. One-way ANOVA with Kruskal-Wallis test followed by
831 Dunn's test for multiple comparisons were conducted.
832
833 **Figure S10. Sotrovimab binding to infected cells.** IGROV-1 cells were infected with the indicated virus
834 for 24h. Then, cells were stained with Sotrovimab or the pan-coronavirus anti-S2 mAb10 antibody.
835 After fixation, cells were intracellularly stained with anti-SARS-CoV-2 nucleoprotein (N) antibody NCP-
836 1 and analyzed by flow cytometry. Representative examples of the gating strategy **(a)** and co-staining
837 of Nucleocapsid and Sotrovimab **(b)** or mAb10 **(c). d.** Quantification of SARS-CoV-2 nucleoprotein+ cells
838 (left), Spike+ cells strained with Sotrovimab (middle) and mAb10 (right). One-way ANOVA with Kruskal-
839 Wallis test followed by Dunn's test for multiple comparisons were conducted.
840
841

Acknowledgements

The authors thank Nicoletta Casartelli and Timothée Bruel for careful reading of the manuscript, the patients who participated to this study, the members of the Virus and Immunity Unit and other teams for discussion and help, Julien Puech from Hôpital Europeen Georges Pompidou for organizing the collect and analysis of nasopharyngeal swabs, Hugo Mouquet and Cyril Planchais for the kind gift of reagents, Nathalie Aulner and the staff at the UtechS Photonic BioImaging (UPBI) core facility (Institut Pasteur), a member of the France BioImaging network, for image acquisition and analysis, Fabienne Peira, Vanessa Legros, Aurelie Theillay, Sandra Pallay and Daniela Pires Roteia (CHU Orléans) for their help with the cohorts. The authors thank "the Centre de Ressources biologiques" from Hospices Civils de Lyon (BRIF number: BB-0033-00046), the members of the National Reference Center for viruses of respiratory infections hosted at Institut Pasteur, and the Mutualized platform for Microbiology (P2M). This work has used the computational and storage services (Maestro cluster) provided by the IT department at Institut Pasteur, Paris

Funding

Work in OS lab is funded by Institut Pasteur, Urgence COVID-19 Fundraising Campaign of Institut Pasteur, Fondation pour la Recherche Médicale (FRM), ANRS, the Vaccine Research Institute (ANR-10-LABX-77), Labex IBEID (ANR-10-LABX-62-IBEID), ANR / FRM Flash Covid PROTEO-SARS-CoV-2, ANR Coronamito, HERA european funding, Sanofi and IDISCOVR. DP is supported by the Vaccine Research Institute. The E.S.-L. laboratory is funded by Institut Pasteur, the INCEPTION program (Investissements d'Avenir grant ANR-16-CONV-0005), the Ixcore foundation for research, the French Government's Investissement d'Avenir programme, Laboratoire d'Excellence 'Integrative Biology of Emerging Infectious Diseases' (grant no. ANR-10-LABX-62-IBEID), the HERA Project DURABLE (grant no 101102733) and the NIH PICREID (grant no U01AI151758). The Opera system was co-funded by Institut Pasteur and the Région ile de France (DIM1Health). Work in UPBI is funded by grant ANR-10-INSB-04-01 and Région Ile-de-France program DIM1-Health. The funders of this study had no role in study design, data collection, analysis and interpretation, or writing of the article.

Author Contributions Statement

Experimental strategy design, experiments: D.P., I.S., F.P., F.G-B, W.B., M.H., J.B., T.V., O.S.
Vital materials: F.D., P.R., D.V., H.P., B.L., S.T-A. L.H., T.P., E.S-L.
Phylogenetic analysis: F.L., E.S-L.
Viral sequencing: M.P., D.V., H.P., B.L., E.S-L.
Manuscript writing and editing: D.P., E.S-L., O.S.

Competing Interests Statement

879 The authors declare no competing interests.
880
881 **References**
882
883

884 1. Viana, R.*, et al.* Rapid epidemic expansion of the SARS-CoV-2 Omicron variant in
885 southern Africa. *Nature* **603**, 679-686 (2022).
886 2. Tegally, H.*, et al.* Emergence of SARS-CoV-2 Omicron lineages BA.4 and BA.5 in South
887 Africa. *Nature Medicine* **28**, 1785-1790 (2022).
888 3. Andrews, N.*, et al.* Covid-19 Vaccine Effectiveness against the Omicron (B.1.1.529)
889 Variant. *New England Journal of Medicine* **386**, 1532-1546 (2022).
890 4. Abu-Raddad, L.J.*, et al.* Effect of mRNA Vaccine Boosters against SARS-CoV-2 Omicron
891 Infection in Qatar. *New England Journal of Medicine* **386**, 1804-1816 (2022).
892 5. Kuhlmann, C.*, et al.* Breakthrough infections with SARS-CoV-2 omicron despite mRNA
893 vaccine booster dose. *The Lancet* **399**, 625-626 (2022).
894 6. Lin, D.-Y.*, et al.* Durability of Bivalent Boosters against Omicron Subvariants. *New*
895 *England Journal of Medicine* (2023).
896 7. Miller, J.*, et al.* Substantial Neutralization Escape by SARS-CoV-2 Omicron Variants
897 BQ.1.1 and XBB.1. *New England Journal of Medicine* (2023).
898 8. Wang, Q.*, et al.* Alarming antibody evasion properties of rising SARS-CoV-2 BQ and XBB
899 subvariants. *Cell* (2022).
900 9. Barnes, C.O.*, et al.* SARS-CoV-2 neutralizing antibody structures inform therapeutic
901 strategies. *Nature* **588**, 682-687 (2020).
902 10. Gruell, H.*, et al.* Antibody-mediated neutralization of SARS-CoV-2. *Immunity* **55**, 925-
903 944 (2022).
904 11. Cao, Y.*, et al.* Imprinted SARS-CoV-2 humoral immunity induces convergent Omicron
905 RBD evolution. *Nature*, https://doi.org/10.1038/s41586-41022-05644-41587 (2022).
906 12. Park, Y.-J.*, et al.* Imprinted antibody responses against SARS-CoV-2 Omicron
907 sublineages. *Science* **0**, eadc9127 (2022).
908 13. Crotty, S. Hybrid immunity. *Science* **372**, 1392-1393 (2021).
909 14. Pulliam, J.R.C.*, et al.* Increased risk of SARS-CoV-2 reinfection associated with
910 emergence of Omicron in South Africa. *Science* **376**, eabn4947 (2022).
911 15. WHO. Tracking SARS-CoV-2 variants. *https://www.who.int/activities/tracking-SARS-*
912 *CoV-2-variants* (2023).
913 16. Uriu, K.*, et al.* Transmissibility, infectivity, and immune evasion of the SARS-CoV-2
914 BA.2.86 variant. *The Lancet Infectious Diseases* (2023).
915 17. Reeve, L.*, et al.* High attack rate in a large care home outbreak of SARS-CoV-2 BA.2.86,
916 East of England, August 2023. *Eurosurveillance* **28**, 2300489 (2023).
917 18. Herder, V.*, et al.* The SARS-CoV-2 Omicron sub-variant BA.2.86 is attenuated in
918 hamsters. *Biorxiv*, 2023.2011.2010.566576 (2023).
919 19. Tamura, T.*, et al.* Virological characteristics of the SARS-CoV-2 BA.2.86 variant. *Biorxiv*,
920 2023.2011.2002.565304 (2023).
921 20. Tamura, T.*, et al.* Virological characteristics of the SARS-CoV-2 BA.2.86 variant. *Cell*
922 *Host & Microbe*.
923 21. Faraone, J.N.*, et al.* Immune Evasion and Membrane Fusion of SARS-CoV-2 XBB
924 Subvariants EG.5.1 and XBB.2.3. *Biorxiv*, 2023.2008.2030.555188 (2023).
925 22. Hu, Y.*, et al.* Less neutralization evasion of SARS-CoV-2 BA.2.86 than XBB sublineages
926 and CH.1.1. *Biorxiv*, 2023.2009.2010.557047 (2023).

927 23. Khan, K., *et al.* Evolution and neutralization escape of the SARS-CoV-2 BA.2.86
928 subvariant. *medRxiv*, 2023.2009.2008.23295250 (2023).
929 24. Lasrado, N., *et al.* Neutralization escape by SARS-CoV-2 Omicron subvariant BA.2.86.
930 *Vaccine* **41**, 6904-6909 (2023).
931 25. Lassauniere, R., *et al.* Neutralisation of SARS-CoV-2 Omicron subvariants BA.2.86 and
932 EG.5.1 by antibodies induced by earlier infection or vaccination. *Biorxiv*,
933 2023.2010.2001.560365 (2023).
934 26. Qu, P., *et al.* Immune evasion, infectivity, and fusogenicity of SARS-CoV-2 BA.2.86 and
935 FLip variants. *Cell* (2024).
936 27. Sheward, D.J., *et al.* Sensitivity of BA.2.86 to prevailing neutralising antibody
937 responses. *Biorxiv*, 2023.2009.2002.556033 (2023).
938 28. Wang, Q., *et al.* Antigenicity and receptor affinity of SARS-CoV-2 BA.2.86 spike. *Nature*
939 (2023).
940 29. Yang, S., *et al.* Antigenicity and infectivity characterisation of SARS-CoV-2 BA.2.86. *The*
941 *Lancet Infectious Diseases* (2023).
942 30. Wang, Q., *et al.* Antibody Neutralization of Emerging SARS-CoV-2: EG.5.1 and XBC.1.6.
943 *Biorxiv*, 2023.2008.2021.553968 (2023).
944 31. Zhang, L., *et al.* SARS-CoV-2 BA.2.86 enters lung cells and evades neutralizing
945 antibodies with high efficiency. *Cell*. (2023)
946 32. Murrell, B. https://github.com/MurrellGroup/lineages. (2023).
947 33. Yang, S., *et al.* Fast evolution of SARS-CoV-2 BA.2.86 to JN.1 under heavy immune
948 pressure. *Biorxiv*, 2023.2011.2013.566860 (2023).
949 34. Uraki, R., *et al.* Characterization of an EG.5.1 clinical isolate in vitro and
950 in vivo. *Biorxiv*, 2023.2008.2031.555819 (2023).
951 35. Yue, C., *et al.* Enhanced transmissibility of XBB.1.5 is contributed by both strong ACE2
952 binding and antibody evasion. *Biorxiv*, 2023.2001.2003.522427 (2023).
953 36. Planas, D., *et al.* Resistance of Omicron subvariants BA.2.75.2, BA.4.6, and BQ.1.1 to
954 neutralizing antibodies. *Nature Communications* **14**, 824 (2023).
955 37. Heurich, A., *et al.* TMPRSS2 and ADAM17 Cleave ACE2 Differentially and Only
956 Proteolysis by TMPRSS2 Augments Entry Driven by the Severe Acute Respiratory
957 Syndrome Coronavirus Spike Protein. *Journal of Virology* **88**, 1293-1307 (2014).
958 38. Matsuyama, S., *et al.* Enhanced isolation of SARS-CoV-2 by TMPRSS2-expressing cells.
959 *Proceedings of the National Academy of Sciences* **117**, 7001-7003 (2020).
960 39. Koch, J., *et al.* TMPRSS2 expression dictates the entry route used by SARS-CoV-2 to
961 infect host cells. *The EMBO Journal* **40**, e107821 (2021).
962 40. Meng, B., *et al.* Altered TMPRSS2 usage by SARS-CoV-2 Omicron impacts infectivity and
963 fusogenicity. *Nature* **603**, 706-714 (2022).
964 41. Mykytyn, A.Z., *et al.* SARS-CoV-2 Omicron entry is type II transmembrane serine
965 protease-mediated in human airway and intestinal organoid models. *Journal of*
966 *Virology* **97**, e00851-00823 (2023).
967 42. Buchrieser, J., *et al.* Syncytia formation by SARS-CoV-2-infected cells. *EMBO J* **39**,
968 e106267 (2020).
969 43. Rajah, M.M., *et al.* SARS-CoV-2 Alpha, Beta, and Delta variants display enhanced Spike-
970 mediated syncytia formation. *The EMBO Journal* **n/a**, e108944 (2021).
971 44. Bolland, W., *et al.* High fusion and cytopathy of SARS-CoV-2 variant B.1.640.1. *Journal*
972 *of Virology* **0**, e01351-01323 (2023).

973 45. Suzuki, R., *et al.* Attenuated fusogenicity and pathogenicity of SARS-CoV-2 Omicron
974 variant. *Nature* **603**, 700-705 (2022).
975 46. Mlcochova, P., *et al.* SARS-CoV-2 B.1.617.2 Delta variant replication and immune
976 evasion. *Nature* **599**, 114-119 (2021).
977 47. Robinot, R., *et al.* SARS-CoV-2 infection induces the dedifferentiation of multiciliated
978 cells and impairs mucociliary clearance. *Nature Communications* **12**, 4354 (2021).
979 48. Willett, B.J., *et al.* SARS-CoV-2 Omicron is an immune escape variant with an altered
980 cell entry pathway. *Nature Microbiology* **7**, 1161-1179 (2022).
981 49. WHO. Therapeutics and COVID-19: living guideline. Sept 16, 2022 Update
982 https://www.who. *int/publications/i/item/WHO-2019-nCoV- therapeutics-2022.5*
983 (2022).
984 50. Bruel, T., *et al.* Sotrovimab therapy elicits antiviral activities against Omicron BQ.1.1
985 and XBB.1.5 in sera of immunocompromised patients. *Med* **4**, 664-667 (2023).
986 51. Addetia, A., *et al.* Neutralization, effector function and immune imprinting of Omicron
987 variants. *Nature* **621**, 592-601 (2023).
988 52. Ragonnet-Cronin, M., *et al.* Generation of SARS-CoV-2 escape mutations by
989 monoclonal antibody therapy. *Nature Communications* **14**, 3334 (2023).
990 53. France, S.p. Point épidémiologique COVID-19 du 10 février 2022. .
991 https://www.santepubliquefrance.fr/presse/2022/point-epidemiologique-covid-19-
992 du-10-fevrier-2022-le-ralentissement-de-la-circulation-du-sars-cov-2-se-confirme-et-
993 s-accompagne-d-une-baisse-des (2022).
994 54. Planas, D., *et al.* Considerable escape of SARS-CoV-2 Omicron to antibody
995 neutralization. *Nature* **602**, 671-675 (2022).
996 55. Planas, D., *et al.* Duration of BA.5 neutralization in sera and nasal swabs from SARS-
997 CoV-2 vaccinated individuals, with or without omicron breakthrough infection. *Med* **3**,
998 838-847.e833 (2022).
999 56. Aggarwal, A., *et al.* TMPRSS2 activation of Omicron lineage Spike glycoproteins is
1000 regulated by TMPRSS2 cleavage of ACE2. *Biorxiv*, 2023.2009.2022.558930 (2023).
1001 57. Yousefi, M., *et al.* Betacoronaviruses SARS-CoV-2 and HCoV-OC43 infections in IGROV-
1002 1 cell line require aryl hydrocarbon receptor. *Emerging Microbes & Infections* **12**,
1003 2256416 (2023).
1004 58. Saunders, N., *et al.* TMPRSS2 is a functional receptor for human coronavirus HKU1.
1005 *Nature* **624**, 207-214 (2023).
1006 59. Cao, Y., *et al.* Characterization of the enhanced infectivity and antibody evasion of
1007 Omicron BA.2.75. *Cell Host & Microbe* **30**, 1527-1539.e1525 (2022).
1008 60. Park, Y.-J., *et al.* Imprinted antibody responses against SARS-CoV-2 Omicron
1009 sublineages. *Science* **378**, 619-627 (2022).
1010 61. Moriyama, S., *et al.* Structural delineation and computational design of SARS-CoV-2-
1011 neutralizing antibodies against Omicron subvariants. *Nature Communications* **14**, 4198
1012 (2023).
1013 62. Chalkias, S., *et al.* Safety and Immunogenicity of XBB.1.5-Containing mRNA Vaccines.
1014 *medRxiv*, 2023.2008.2022.23293434 (2023).
1015 63. Wang, Q., *et al.* XBB.1.5 monovalent mRNA vaccine booster elicits robust neutralizing
1016 antibodies against emerging SARS-CoV-2 variants. *Biorxiv*, 2023.2011.2026.568730
1017 (2023).
1018 64. Krammer, F. & Ellebedy, A.H. Variant-adapted COVID-19 booster vaccines. *Science* **382**,
1019 157-159 (2023).

1020 65. Bouhaddou, M.*, et al.* SARS-CoV-2 variants evolve convergent strategies to remodel
1021 the host response. *Cell* **186**, 4597-4614.e4526 (2023).
1022 66. Bruel, T.*, et al.* Longitudinal analysis of serum neutralization of SARS-CoV-2 Omicron
1023 BA.2, BA.4, and BA.5 in patients receiving monoclonal antibodies. *Cell Reports*
1024 *Medicine*, 100850 (2022).
1025 67. Trouillet-Assant, S.*, et al.* Assessment of serological techniques for screening patients
1026 for COVID-19 (COVID-SER): a prospective, multicentric study. *BMJ Open* **10**, e041268
1027 (2020).
1028 68. Planas, D.*, et al.* Reduced sensitivity of SARS-CoV-2 variant Delta to antibody
1029 neutralization. *Nature* **596**, 276-280 (2021).
1030 69. Bruel, T.*, et al.* Serum neutralization of SARS-CoV-2 Omicron sublineages BA.1 and BA.2
1031 in patients receiving monoclonal antibodies. *Nature Medicine* **28**, 1297-1302 (2022).
1032 70. Planchais, C.*, et al.* Potent human broadly SARS-CoV-2–neutralizing IgA and IgG
1033 antibodies effective against Omicron BA.1 and BA.2. *Journal of Experimental Medicine*
1034 **219**(2022).
1035 71. Planas, D.*, et al.* Sensitivity of infectious SARS-CoV-2 B.1.1.7 and B.1.351 variants to
1036 neutralizing antibodies. *Nature Medicine* **27**, 917-924 (2021).
1037 72. Hadfield, J.*, et al.* Nextstrain: real-time tracking of pathogen evolution. *Bioinformatics*
1038 **34**, 4121-4123 (2018).
1039 73. Jackson, B. gofasta: command-line utilities for genomic epidemiology research.
1040 *Bioinformatics* **38**, 4033-4035 (2022).
1041

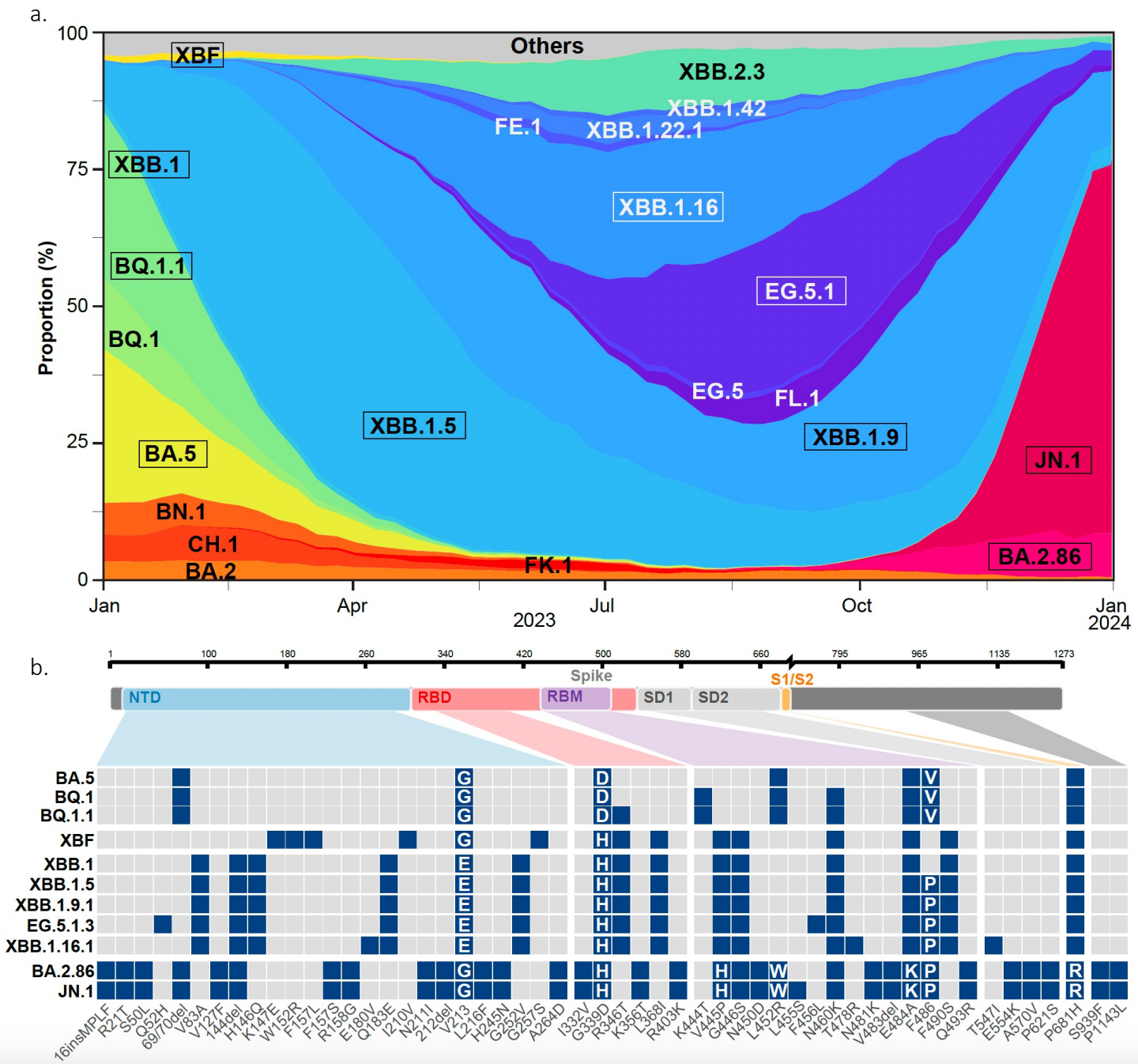

Figure 1. SARS-CoV2 evolution in 2023 and Spike mutation patterns of the main lineages. a. Evolution of the prevalence of main SARS-CoV-2 lineages from January to December 31, 2023. The pattern of emergence and replacement of several lineages, such as XBB.1.5, then XBB.1.9, XBB.1.16 or EG.5.1 and the emergence of BA.2.86 and JN.1 is shown. The variants with a frame are analyzed in this study. b. Changes specific to lineages studied here in comparison to BA.2 are displayed as colored squares. The spike domain organization is displayed on the top, with N-terminal domain (NTD), Receptor Binding Domain (RBD), Receptor Binding Motif (RBM), Single domains SD1 and SD2, S1/S2 cleavage site, and S2 domains. BA.2.86 and its descendant JN.1 show many new mutations compared to other lineages. A complete comparison of spike mutations compared to the reference Wuhan_Hu-1 is presented in Fig. S1b.

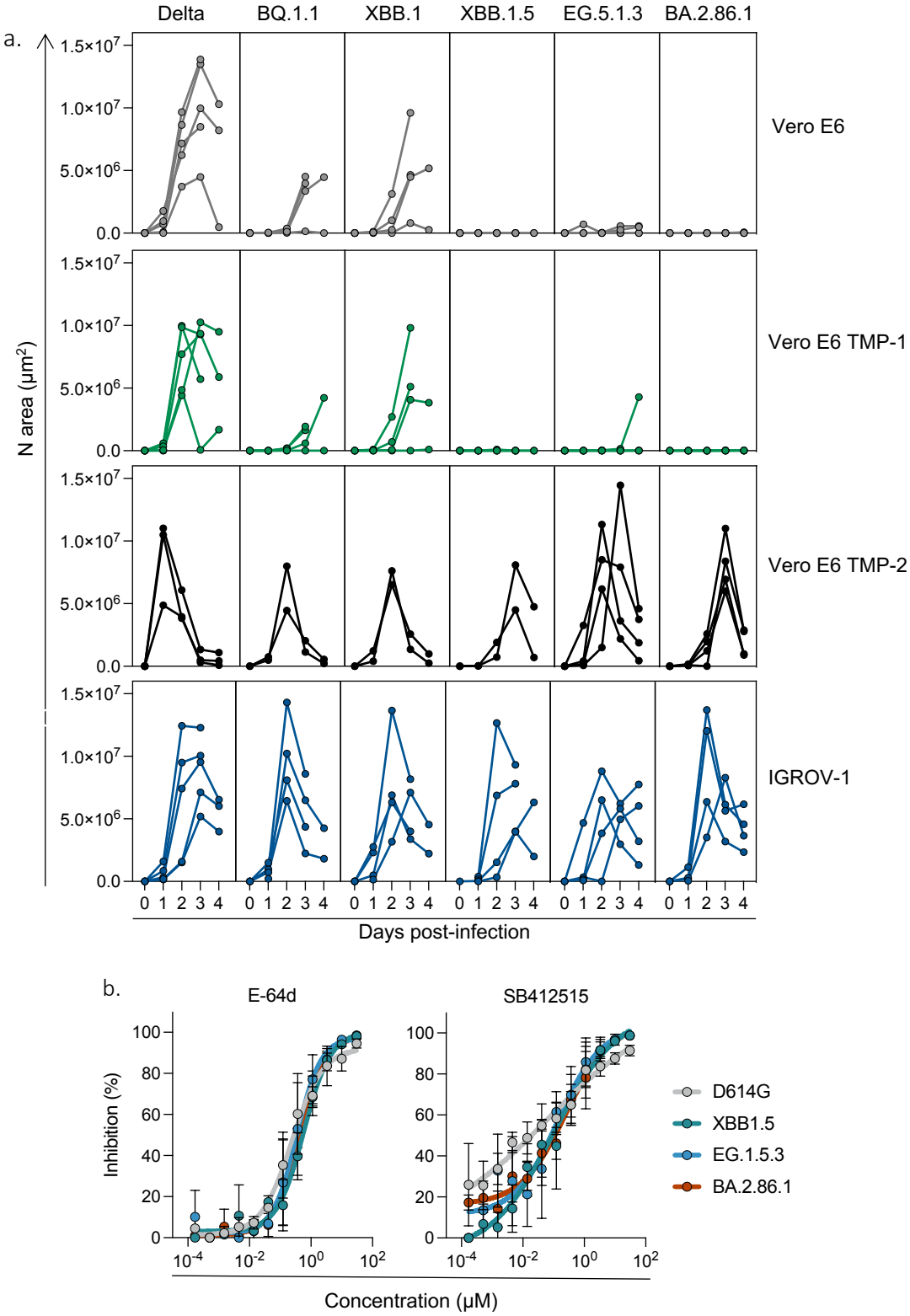

Figure 2. Replication kinetics of SARS-CoV-2 variants in Vero E6, Vero E6 TMP-1 and -2 and IGROV-1 cells. a. Cells were infected with the indicated variants, at $3x10^{-2}$ infectious units per cell. Cells were stained with a pan-coronavirus anti-N antibody at days 1 to 4 pi. The N-positive areas were plotted on the graph. Each curve represents an independent experiment. b. Comparison of the effect of E-64d and SB412515 against different variants. IGROV-1 cells were pre-incubated 2 h with serial dilutions of E-64d or SB412515 (30 to $1.7x10^{-4}$ µM) and infected with D614G, XBB.1.5, EG.5.1.3, or BA.2.86.1. The percentage of inhibition is represented. Data are mean ± s.d. of 3 independent experiments.

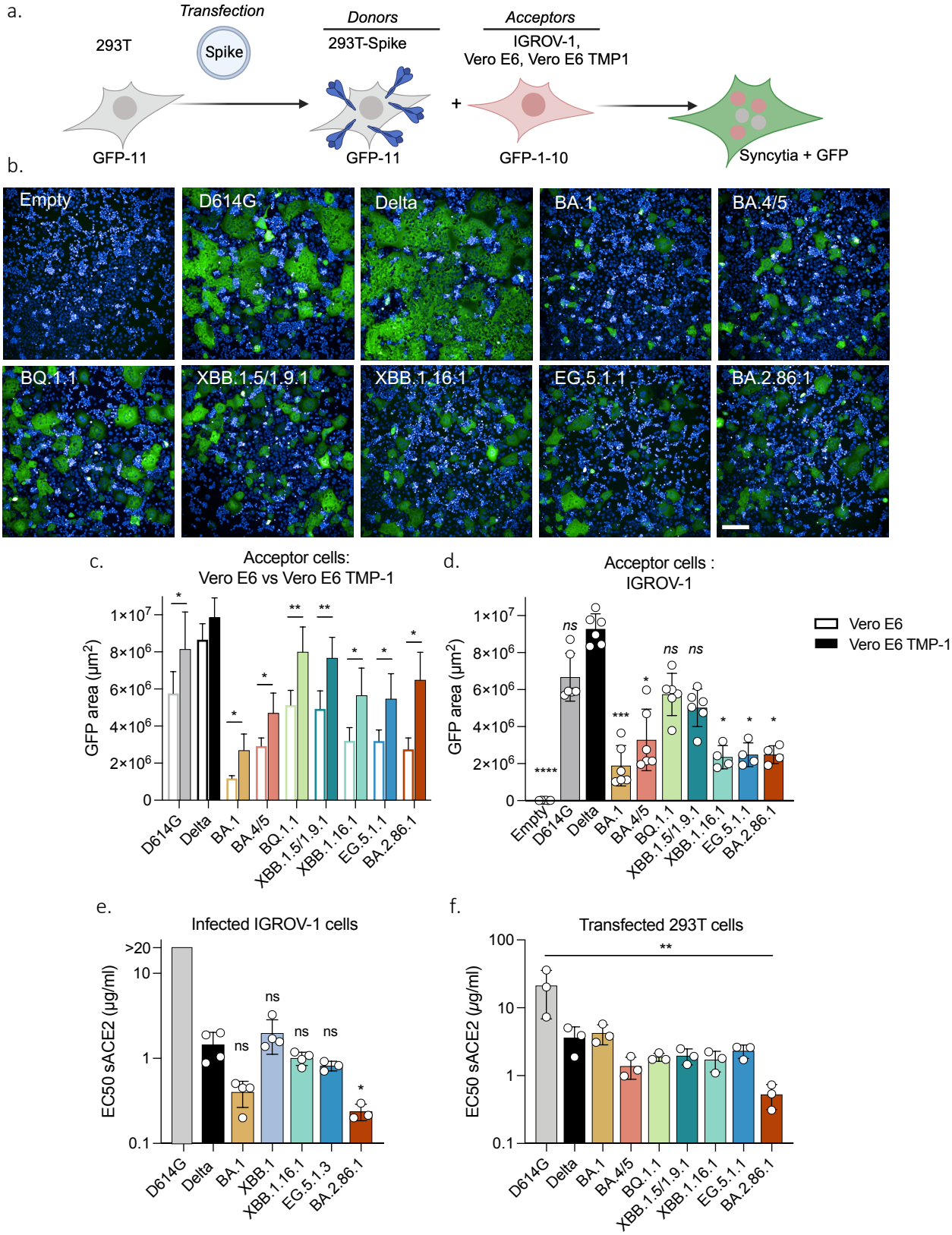
a.
Transfection
293T
Spike
GFP-11
Donors
293T-Spike
GFP-11
Acceptors
IGROV-1,
Vero E6, Vero E6 TMP1
+
GFP-1-10
Syncytia + GFP
b.
Empty
D614G
Delta
BA.1
BA.4/5
BQ.1.1
XBB.1.5/1.9.1
XBB.1.16.1
EG.5.1.1
BA.2.86.1
c.
Acceptor cells:
Vero E6 vs Vero E6 TMP-1
GFP area (µm²)
d.
Acceptor cells :
IGROV-1
Vero E6
Vero E6 TMP-1
e.
Infected IGROV-1 cells
EC50 sACE2 (µg/ml)
f.
Transfected 293T cells
EC50 sACE2 (µg/ml)

Figure 3. Fusogenicity and binding to ACE2 of the variant spike proteins. a. Schematic representation of the coculture system. 293T GFP-11 donor cells were transfected with the indicated variant spike expression plasmids and cocultivated with IGROV-1, Vero E6 or Vero E6 TMP-1 acceptor cells expressing GFP1-10. The area of GFP+ fused cells was measured after 18 h. b. Representative images of cell-cell fusion between 293T donor cells and IGROV-1 acceptor cells. Scale bar, 200 µm. c. Fusogenicity of the different spikes with IGROV-1 acceptor cells. Each dot represents a single experiment. Data are mean ± s.d. of 4-6 independent experiments. One-way ANOVA with Kruskal-Wallis test followed by Dunn's test for multiple comparisons to compare Delta with respective variants were conducted. d. Effect of TMPRSS2 on the fusion of the different spikes. Cell-cell fusion assays were performed with Vero E6 or Vero E6 TMP-1 as target cells. Data are mean ± s.d. of 4 independent experiments. Paired t-test to compare fusion in Vero E6 versus Vero E6 TMP-1 were conducted. e,f. Binding of soluble ACE2 to IGROV-1 infected cells (e) or to 293T cells transiently expressing the Spike (f). Cells were stained with serial dilutions of soluble ACE2. The EC50 of ACE2 binding (µg/ml) for the indicated spike proteins is shown. Data are mean ± s.d. of 3-4 independent experiments. One-way ANOVA with Kruskal-Wallis test followed by Dunn's test for multiple comparisons to compare Delta with respective variants were conducted.

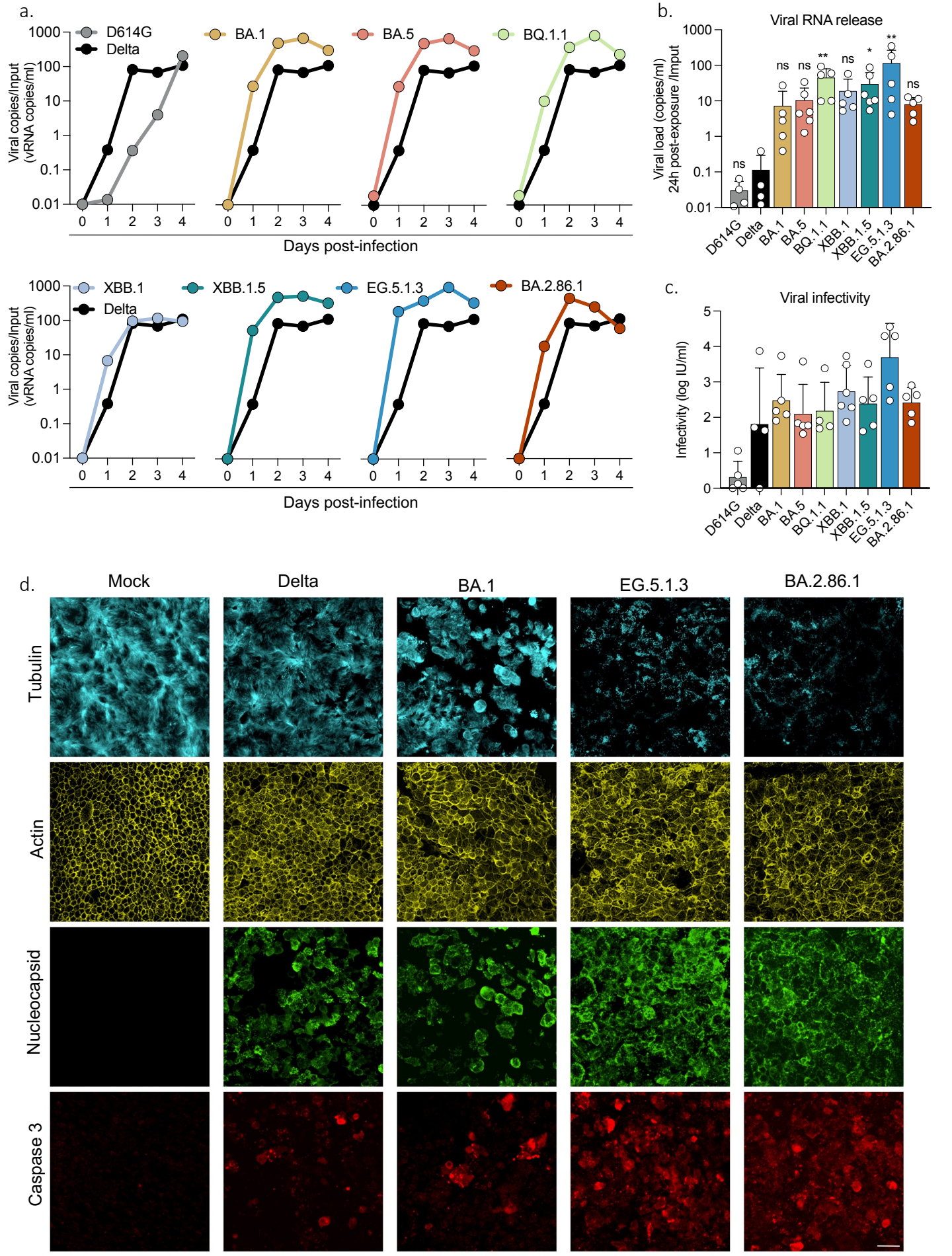
a.
D614G
Delta
BA.1
BA.5
BQ.1.1
Viral copies/Input (vRNA copies/ml)
1000
100
10
1
0.1
0.01
0 1 2 3 4
Days post-infection
XBB.1
XBB.1.5
EG.5.1.3
BA.2.86.1
b.
Viral RNA release
Viral load (copies/ml) 24h post-exposure /Imput
ns
**
*
D614G
Delta
BA.1
BA.5
BQ.1.1
XBB.1
XBB.1.5
EG.5.1.3
BA.2.86.1
c.
Viral infectivity
Infectivity (log IU/ml)
5
4
3
2
1
0
d.
Mock
Delta
BA.1
EG.5.1.3
BA.2.86.1
Tubulin
Actin
Nucleocapsid
Caspase 3

Figure 4. Replication of SARS-CoV-2 variants in hNECs. Primary human nasal epithelial cells (hNECs) cultivated at the air-liquid interface (ALI) were exposed to the indicated SARS-CoV-2 variants. a. Viral RNA release from the apical side of hNECs was measured by RT-qPCR every day up to 4 days p.i.. Replication kinetics of each variant from one representative experiment are represented. b. Comparison of viral RNA release at day 1 pi with the indicated variants. c. Infectious viral titers in supernatants from the apical side were quantified with S-Fuse cells at day 2 p.i. b,c. Data are mean ± s.d. of 4-6 independent experiments. One-way ANOVA with Kruskal-Wallis test followed by Dunn's test for multiple comparisons to compare Delta with respective variants were conducted. d. Immunofluorescence of hNECs stained for tubulin (cyan), actin (yellow), SARS-CoV-2 Nucleocapsid (green) and cleaved caspase-3 (red). Shown is one representative field (150x150 mm) of each variant. Scale bar = 20 µm.

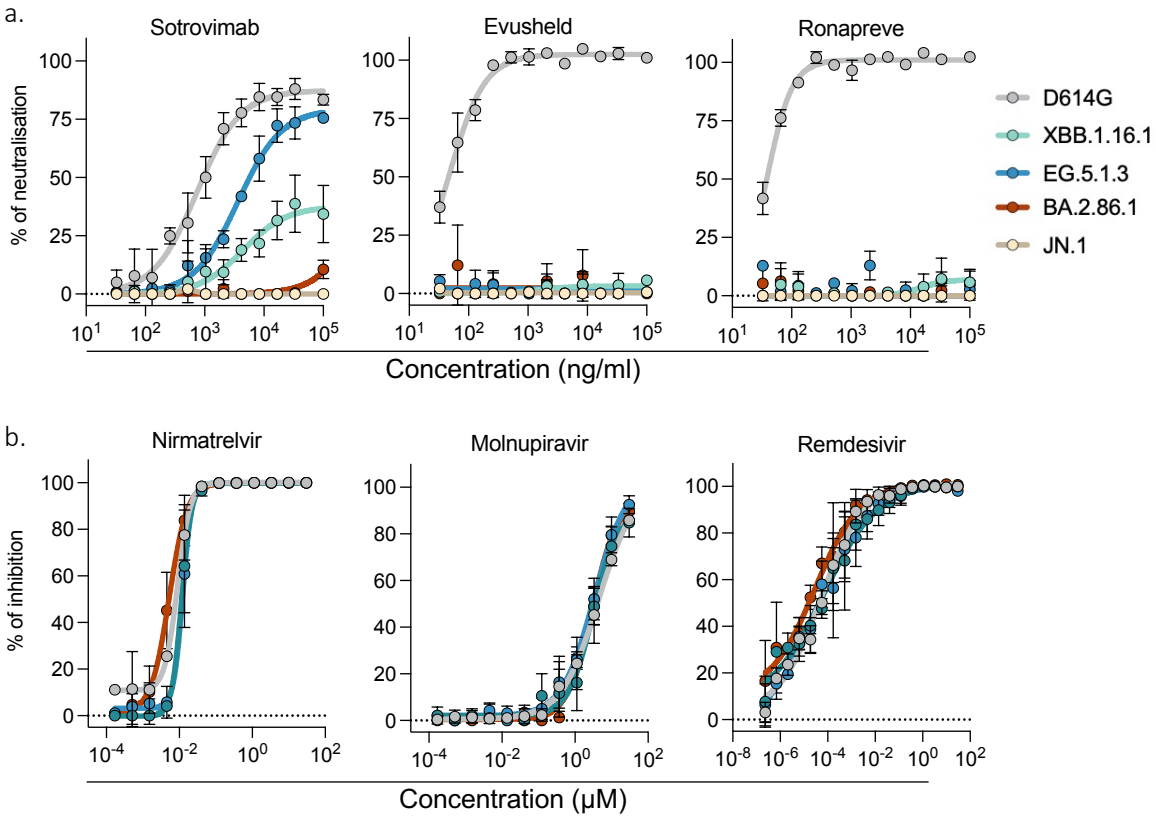

Figure 5. Activity of neutralizing mAbs and antiviral drugs against SARS-CoV-2 variants. a. Neutralization curves of previously approved mAbs. Dose–response analysis of neutralization of the indicated variants by Sotrovimab, Evusheld (Cilgavimab and Tixagevimab) and Ronapreve (Casirivimab and Imdevimab). b. Inhibitory curves of antiviral drugs against the indicated variants. Dose-response analysis of the antiviral effect of Nirmatrelvir, Remdesivir and Molnupiravir. a,b. Data are mean ± s.d. of 3 independent experiments.

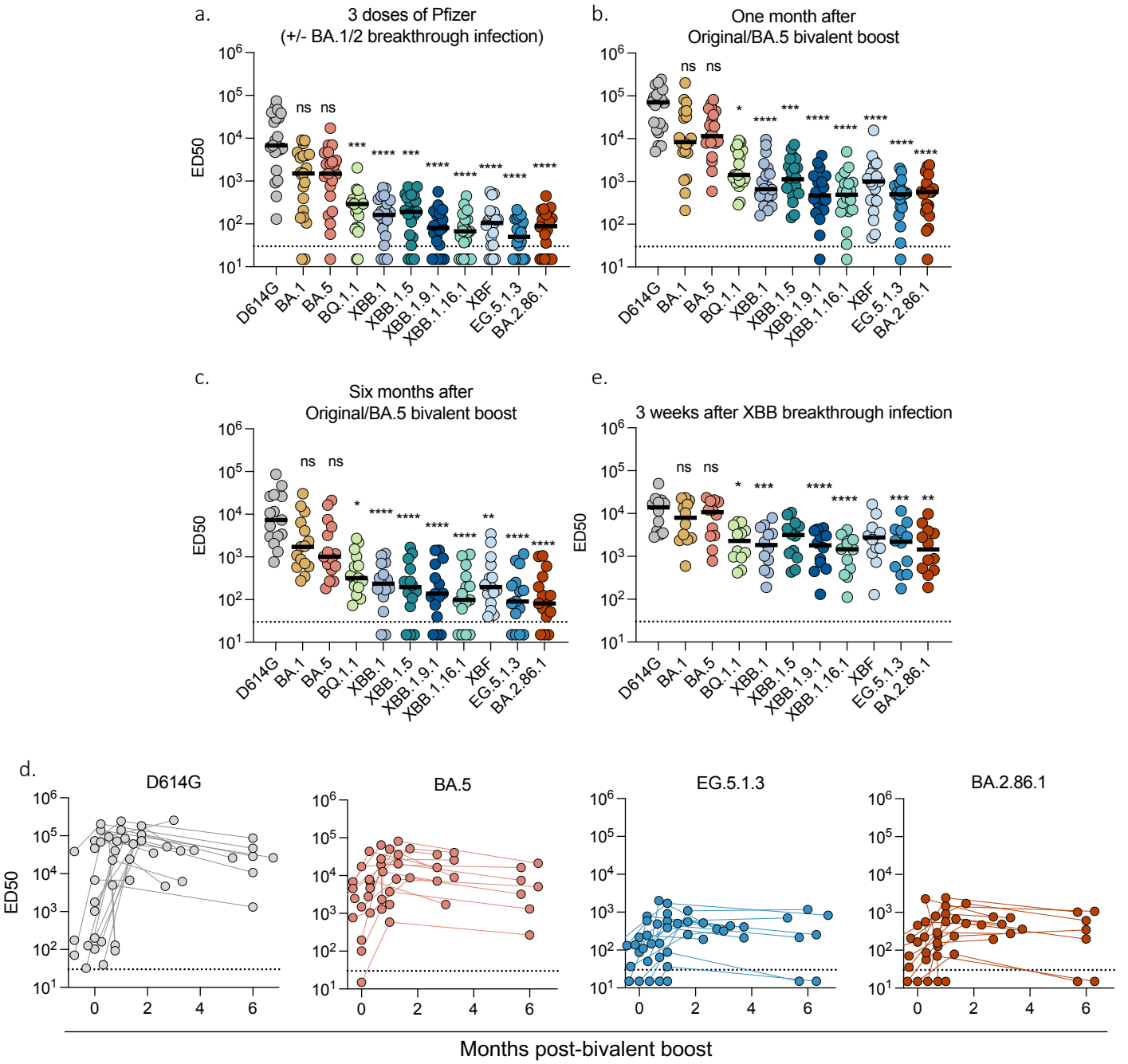

Figure 6. Sensitivity of SARS-CoV-2 variants to sera of vaccinated and/or infected individuals.
Neutralization titers of the sera against the indicated viral variants are expressed as ED50. **a.** Neutralizing activity of sera from individuals vaccinated with 3 doses of Pfizer vaccine. Sera (n= 21) were sampled 25 – 475 days after the third dose. 13/21 had a breakthrough infection at the time of BA.1/2 circulation. **b,c.** Neutralizing activity of sera from individuals having received the bivalent Wuhan/BA.5 Pfizer boost. Sera were sampled one month (b; n= 20) and six months (c; n=14) after the booster dose. **d.** Temporal evolution of Neutralizing Antibody (Nab) titers against D614G, BA.5, EG.5.1.3 and BA.2.86.1 after bivalent Wuhan/BA.5 booster dose. The Nab titers were calculated at the time of injection (month 0) and at the indicated months after injection. **e.** Neutralizing activity of sera from Pfizer-vaccinated recipients after XBB-derived breakthrough infections (infections occurred in September 2023, when XBB-derived variants were predominantly circulating in France). Sera were sampled 10 to 50 days after the breakthrough (n=12). The dotted line indicates the limit of detection (ED50 = 30). Each dot represents the mean of n=2 independent experiments. Black lines represent the median values. Two-sided Friedman test with Dunn's test for multiple comparisons was performed to compare each viral strain to D614G.

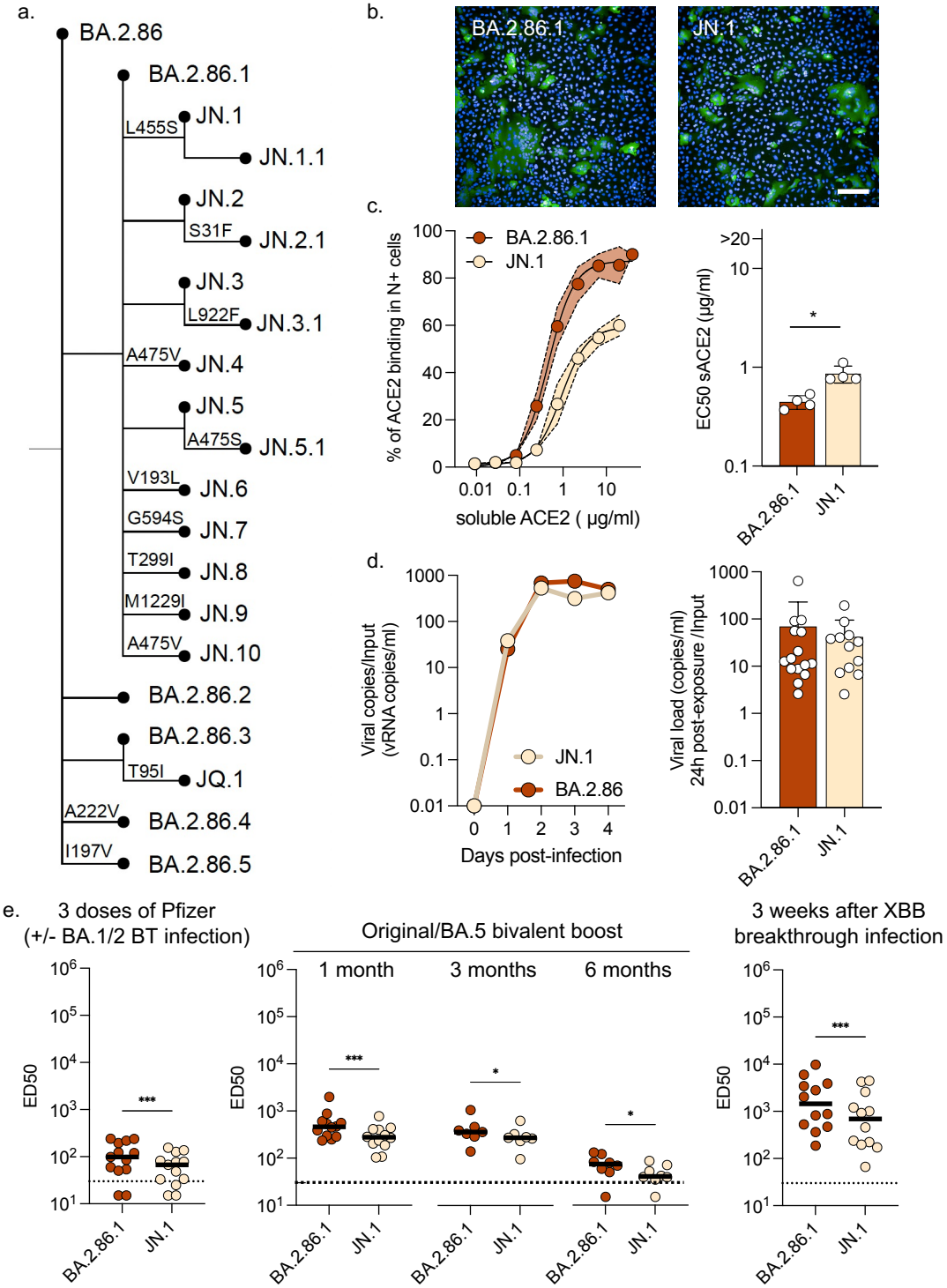

Figure 7. Comparative analysis of BA.2.86.1 and JN.1 variants. a. Schematic tree describing BA.2.86 expanding diversity. Only substitutions in the spike are noted on branches. b. Representative images of cell-cell fusion in S-Fuse cells after infection with BA.2.86.1 and JN.1. Scale bar, 200 µm. c. Binding of soluble ACE2 to IGROV-1 infected cells. Infected cells were stained with serial dilutions of soluble hACE2 (left panel). The EC50 of ACE2 (in µg/ml) is displayed (right panel). Data are from two independent experiments in duplicate. d. Viral RNA release from the apical side of hNECs was measured by RT-qPCR every day up to 4 days p.i.. Replication kinetics of BA.86.1 and JN.1 variants from one representative experiment out of 2 are represented (left). Comparison of viral RNA release at day 1 pi with the indicated variants (right). e. Comparison of neutralization titers against BA.2.86.1 and JN.1 in sera from individuals in the Orléans cohort. Neutralizing activity of sera (n=13) from individuals vaccinated with 3 doses of Pfizer original vaccine, sampled 25-475 days after the third dose (left panel). 9/13 had a breakthrough infection at the time of BA.1/2 circulation. Neutralization activity of sera from recipients of a bivalent Wuhan/BA.5 booster dose. Sera were sampled at 1 (n=12), 3 (n=7) and 6 (n=8) months after the booster dose (middle panel). Neutralization activity of sera from Pfizer-vaccinated individuals with a breakthrough infection in September 2023, when XBB-derived variants were predominantly circulating in France (n=12) (right panel). Sera were sampled 10 to 50 days post-breakthrough infection. The dotted line indicates the limit of detection (ED50 = 30). Each dot represents the mean of n=2 independent experiments. Black lines represent the median values. c,d,e, Paired t-tests were conducted.

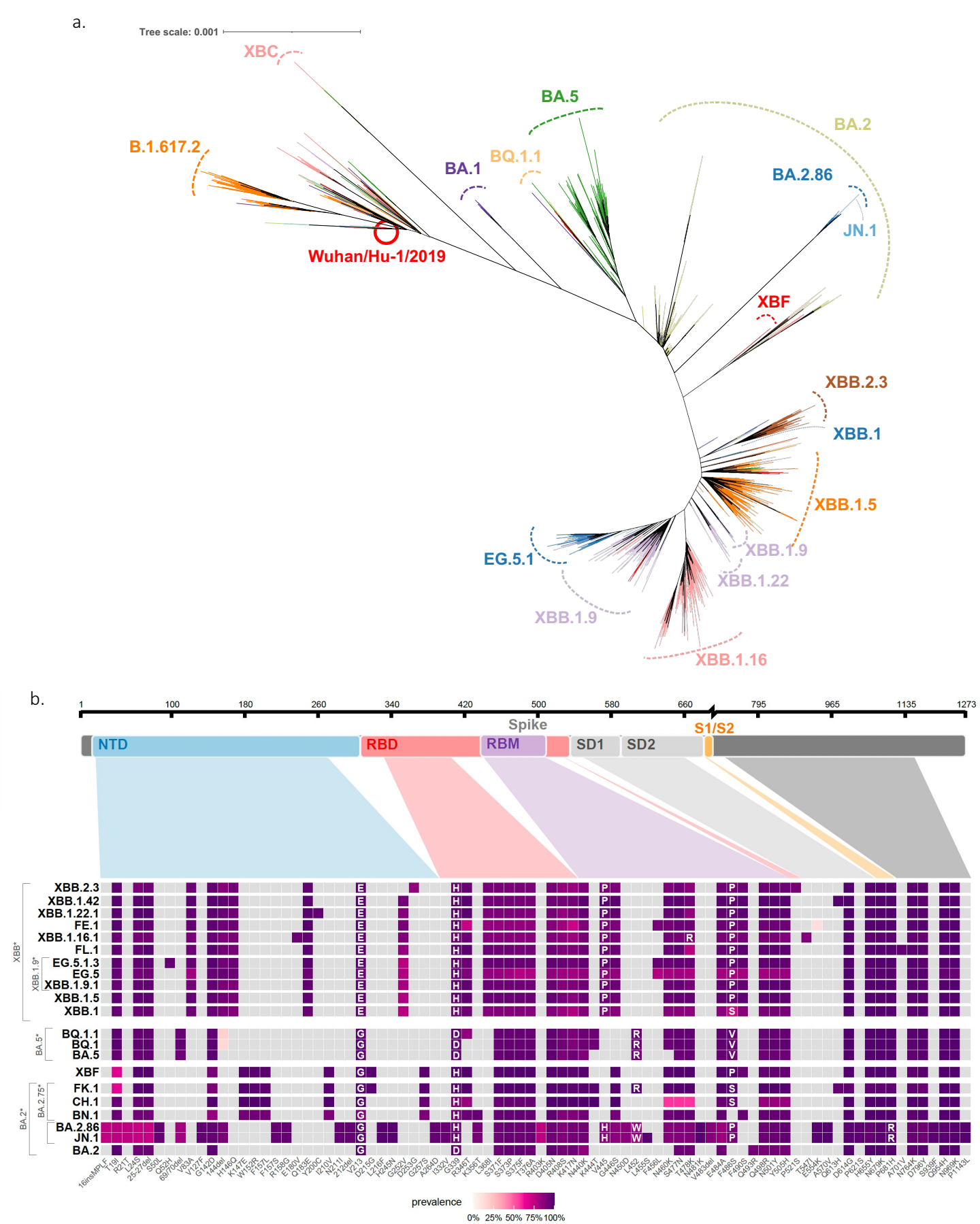

Figure S1. Maximum likelihood phylogeny representing the evolution of the main lineages of SARS-CoV-2 since the beginning of the epidemic. **a.** The red circle indicates one of the first sequences (Wuhan/Hu-1/2019). The BA.2.86 sequences are located inside the BA.2 clade, at the end of a long branch. Of note, a limitation of the inferred phylogeny is that known recombinant lineages (e.g. XBF or XBB) were included in the dataset, and their branching should be interpreted with caution. **b.** Comparison of spike mutations compared to the reference Wuhan_Hu-1 for selected SARS-CoV-2 variants. The color scale reflects the frequency of the mutations within lineages based on the data available on the GISAID EpiCoV database.

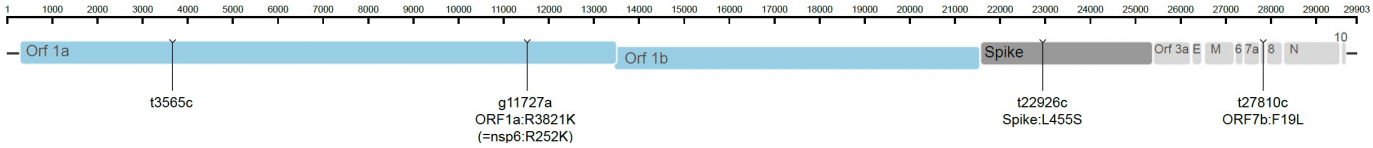

Figure S2. Additional mutations defining lineage JN.1 in comparison to its parent lineage BA.2.86.1. The genome is drawn to scale, and for mutation leading to an amino acid change, the protein is specified.

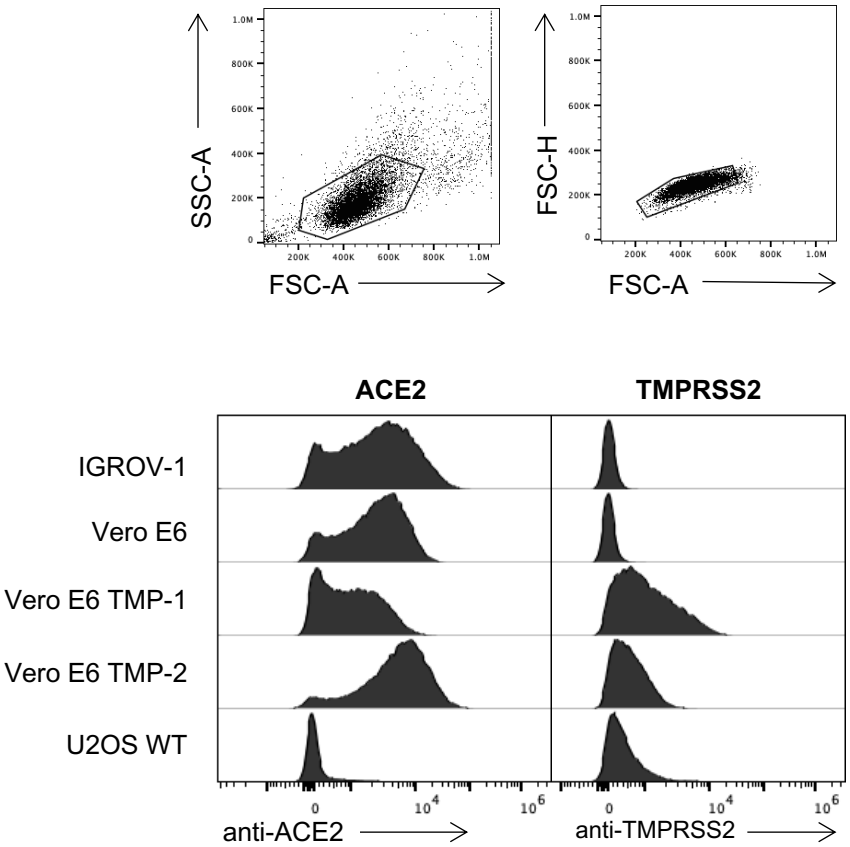

Figure S3. ACE2 and TMPRSS2 expression in cell lines. IGROV-1, Vero E6, Vero E6 TMP-1 and TMP-2 cells were stained with anti-ACE2 or anti-TMPRSS2 antibodies and analyzed by flow cytometry. Representative examples of the gating strategy in IGROV-1 cells and of the signals obtained in cell lines are shown.

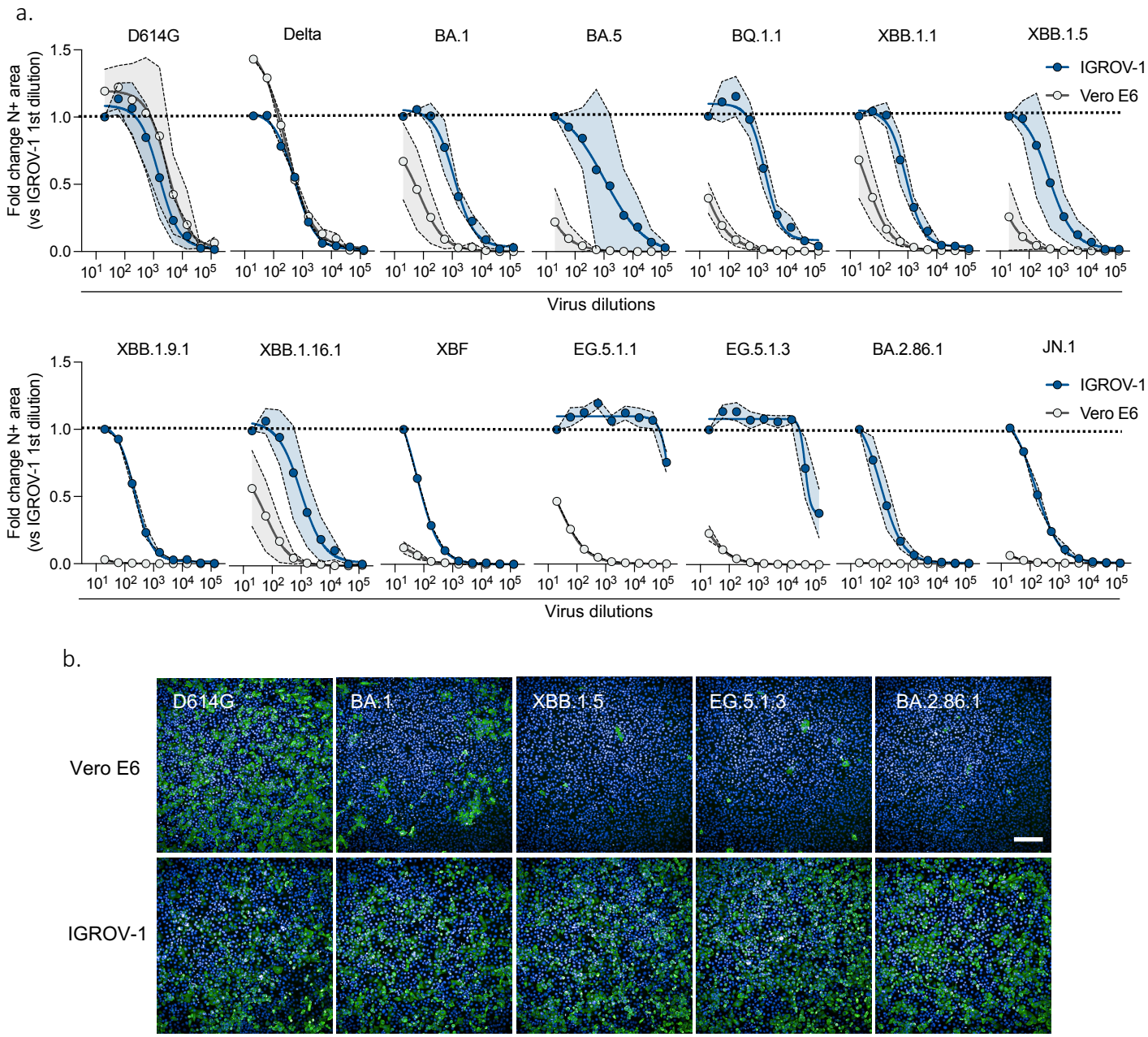

Figure S4. Permissibility of IGROV-1 and Vero E6 cells to SARS-CoV-2 variants. Viral titrations in IGROV-1 and Vero E6 cells. Cells were infected with serial dilutions of the indicated variants. At 24 hours post-infection (p.i.), cells were stained with a pan-coronavirus anti-N antibody (green) and Hoechst to visualize the nuclei (blue). **a.** The N positive areas in IGROV-1 (blue curves) and Vero E6 cells (grey curves) were compared for each viral dilution. The dotted line corresponds to the signal obtained with the first dilution (1/20) in IGROV-1 cells, set to the arbitrary value of 1. Data are mean ± s.d. of 3-5 independent experiments. **b.** Representative images with the indicated viral strains. An identical viral inoculum was used in the two cell lines. Scale bar, 200 µm.

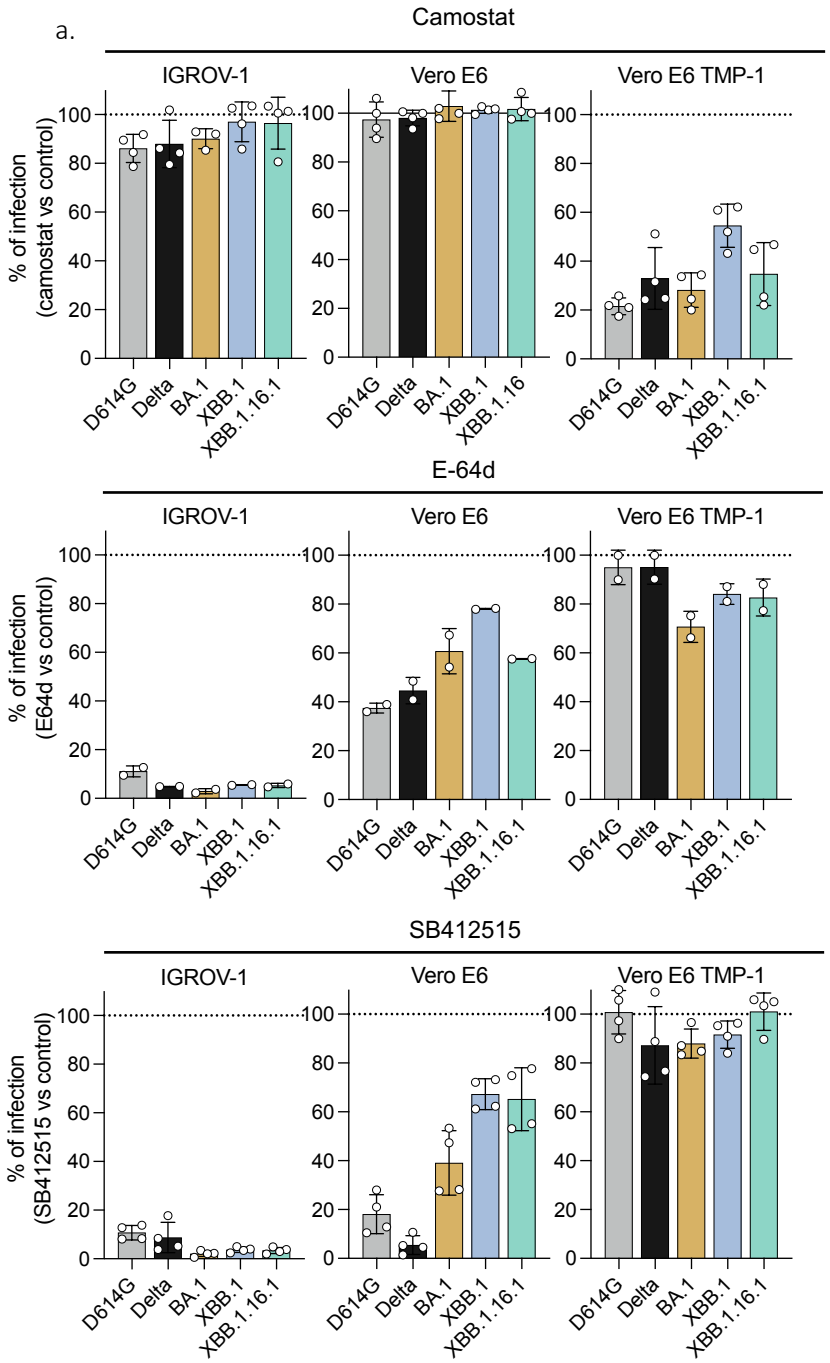

Figure S5. Effect of the TMPRSS2 inhibitor Camostat and Cathepsin L inhibitors E-64d and SB412515 on viral infection a. IGROV-1, Vero E6 and Vero E6 TMP-1 cells pre-incubated 2 h with Camostat (100 µM), E-64d (10 µM), or SB412515 (10 µM) and exposed to the D614G, Delta, BA.1, XBB.1, or XBB.1.16.1 variants for 24 h. The viral inoculum was determined by titration in each cell line to achieve a similar N-positive area at 24 h pi. The cells were stained with a pan-coronavirus anti-N antibody. Hoechst was used to visualize the nuclei for evaluating drug toxicity. The percentage of infection compared to the control (without drugs, represented by the dotted line) is shown. Data are mean ± s.d. of 3 independent experiments.

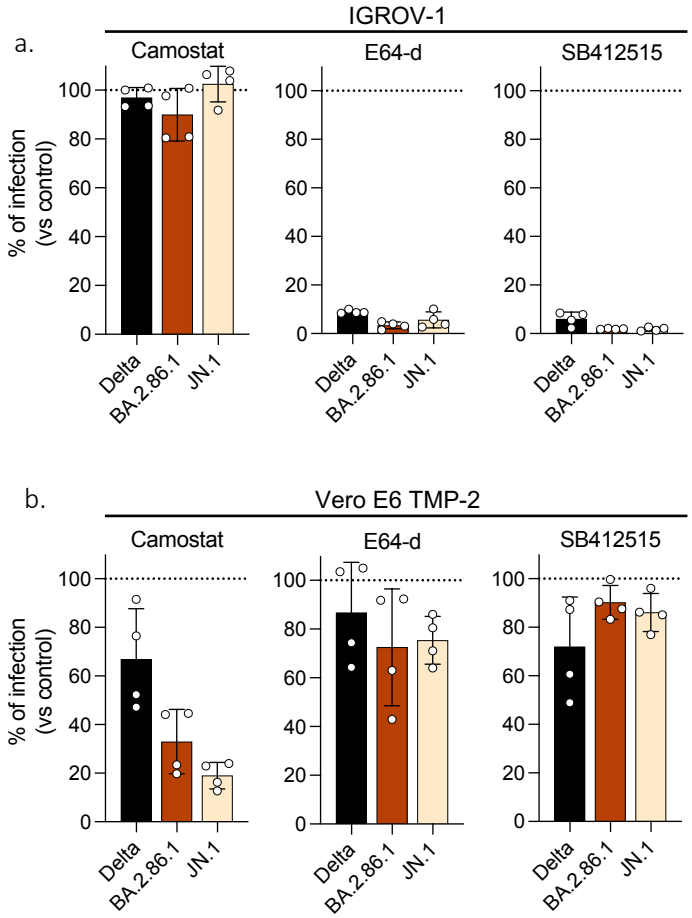

Figure S6. Sensibility of BA.2.86.1 and JN.1 variants to TMPRSS2 inhibitor Camostat and Cathepsin L inhibitors E-64d and SB412515. IGROV-1 **(a)** and Vero E6 TMP-2 **(b)** cells pre-incubated 2 h with Camostat (100 µM), E-64d (10 µM), or SB412515 (10 µM) and exposed to the Delta, BA.2.86.1 and JN.1 variants for 24 h. The viral inoculum was determined by titration in each cell line to achieve a similar N-positive area at 24 h pi. The cells were stained with a pan-coronavirus anti-N antibody. Hoechst was used to visualize the nuclei for evaluating drug toxicity. The percentage of infection compared to the control (without drugs, represented by the dotted line) is shown. Data are mean ± s.d. of 2 independent experiments.

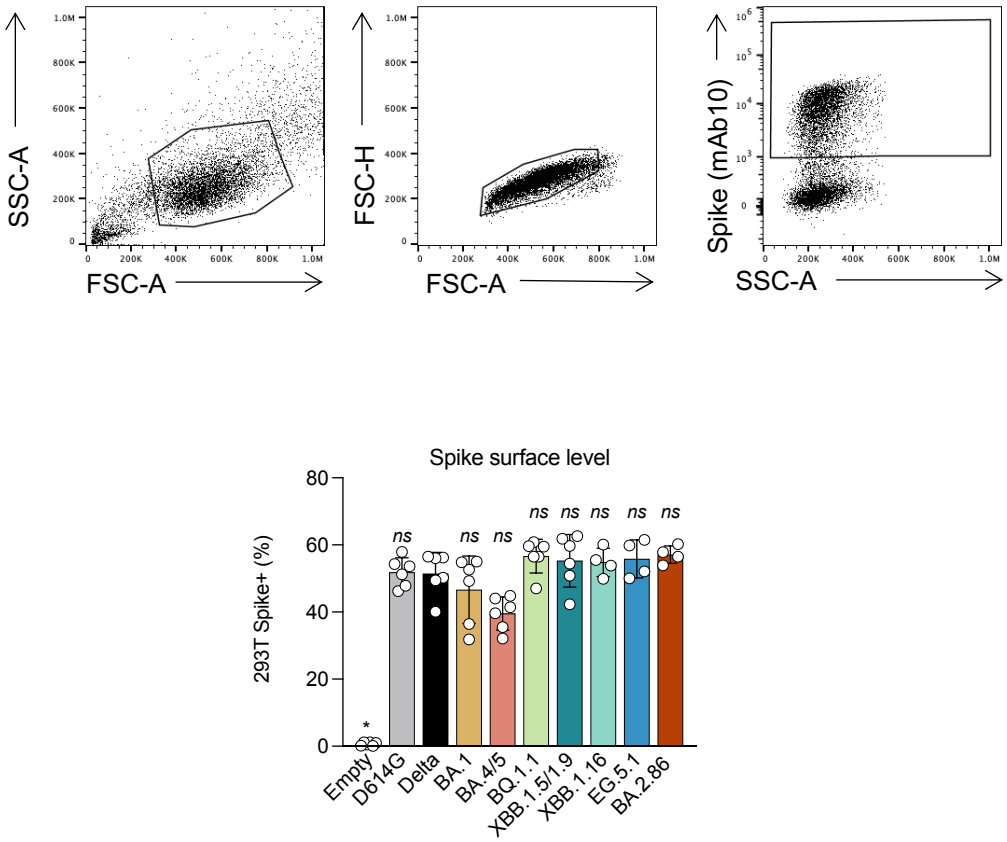

Figure S7. Spike expression in 293T cells. Gating strategy and levels of Spike at the cell surface. 293T cells transiently expressing the indicated variant Spikes were stained with a pan-coronavirus anti-S2 mAb 18 h post-transfection and analyzed by flow cytometry.

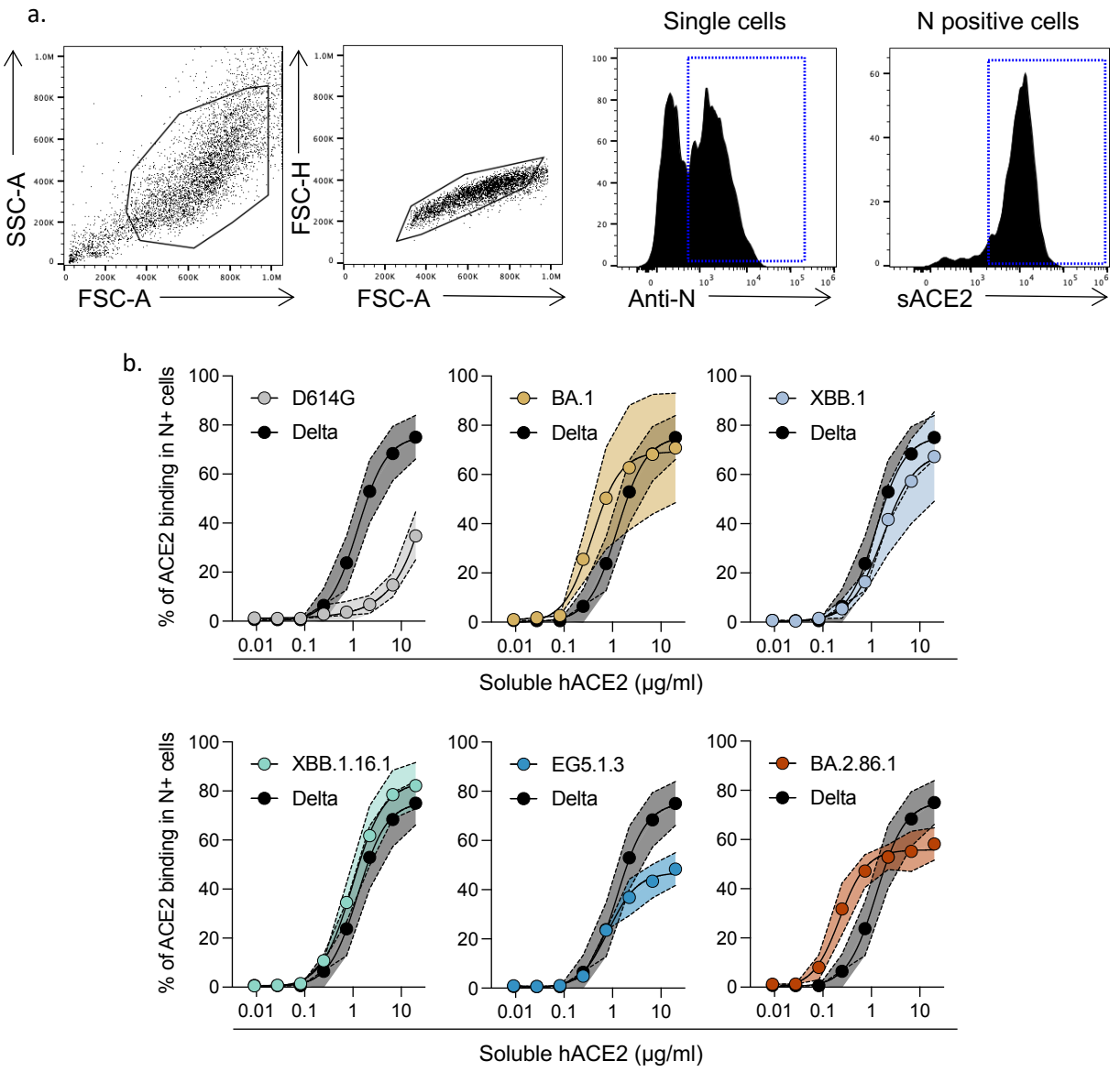

Figure S8. Binding of variant Spike proteins to ACE2. The affinity of the variant Spike proteins expressed at the surface of IGROV-1 infected cells was assessed by staining the cells and flow cytometry analysis. IGROV-1 cells were infected with the indicated variants. a. Representative examples of the gating strategy. b. The percentages of biotinylated hACE2+ cells are represented at various dilutions of hACE2-Fc. Data are mean ± s.d. of 3-4 independent experiments.

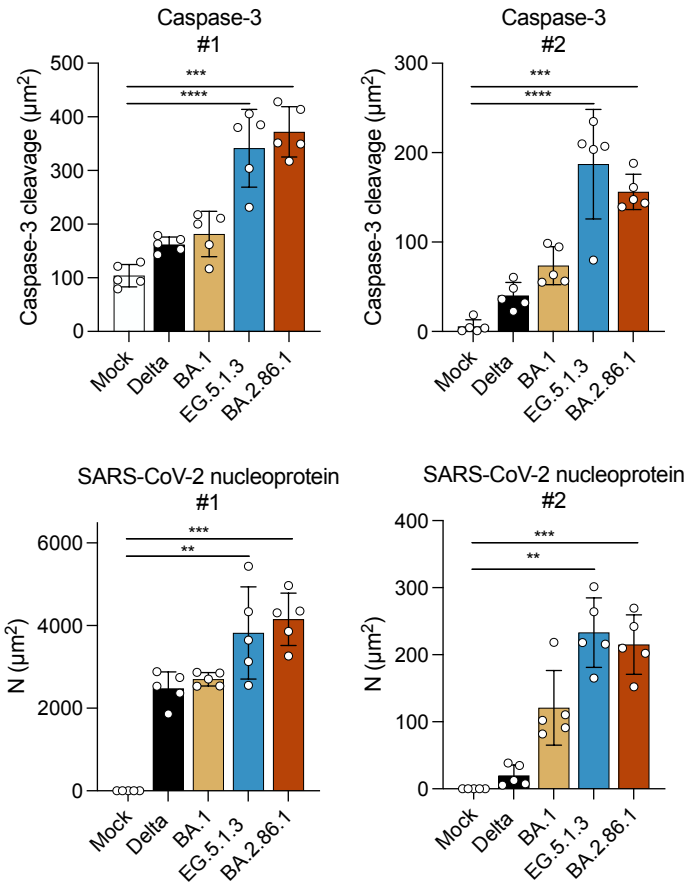

Figure S9. Immunofluorescence of hNECs stained for cleavage products of caspase-3 and SARS-CoV-2 nucleoprotein. Quantification of total area of cleavage products of caspase-3 and SARS-CoV-2 N. Each data point represents one randomly assigned field. One-way ANOVA with Kruskal-Wallis test followed by Dunn's test for multiple comparisons were conducted.

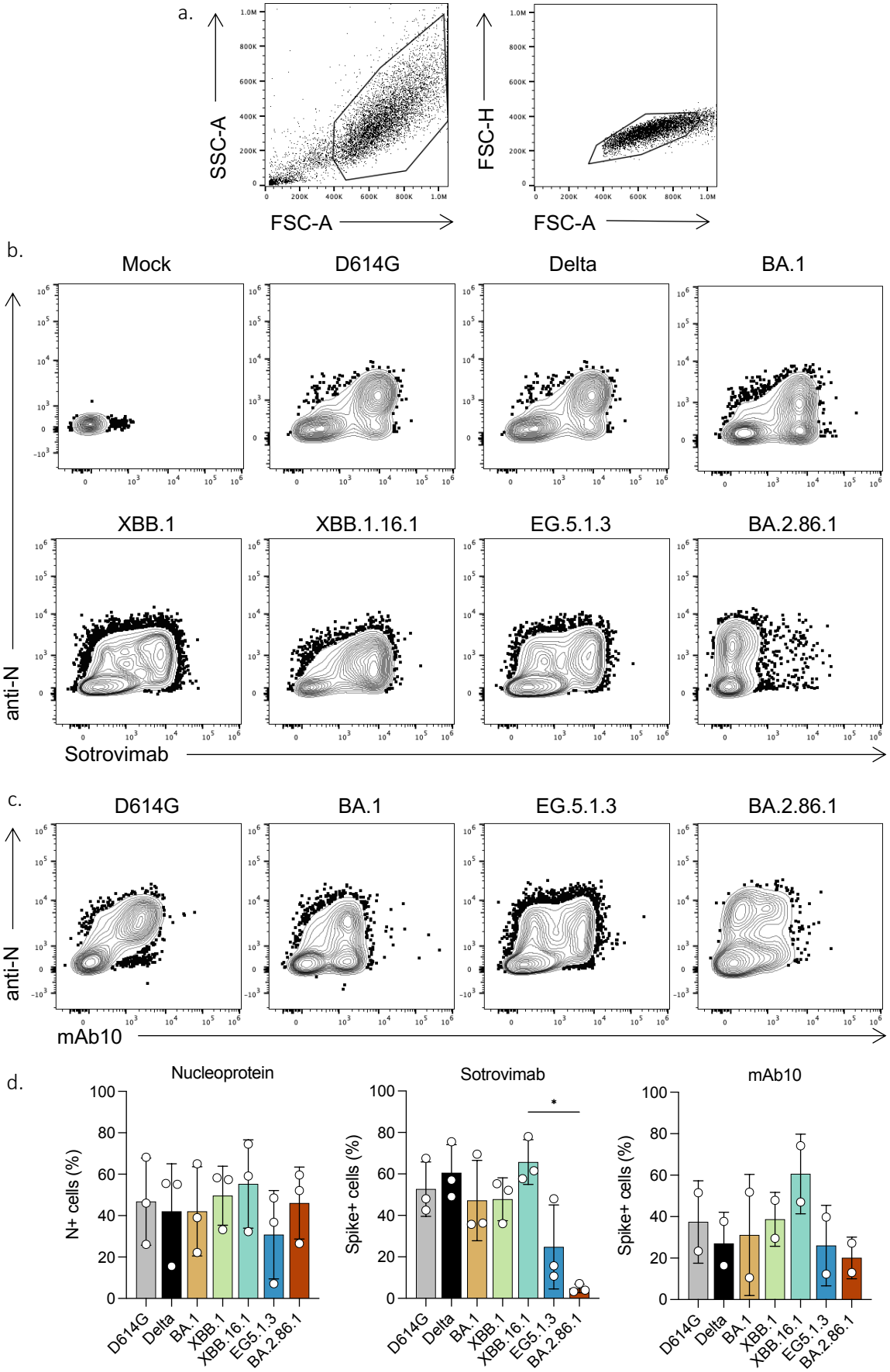

Figure S10. Sotrovimab binding to infected cells. IGROV-1 cells were infected with the indicated virus for 24h. Then, cells were stained with Sotrovimab or the pan-coronavirus anti-S2 mAb10 antibody. After fixation, cells were intracellularly stained with anti-SARS-CoV-2 nucleoprotein (N) antibody NCP-1 and analyzed by flow cytometry. Representative examples of the gating strategy (a) and co-staining of Nucleocapsid and Sotrovimab (b) or mAb10 (c). d. Quantification of the SARS-CoV-2 nucleoprotein+ cells (left), Spike+ cells strained with Sotrovimab (middle) and mAb10 (right). One-way ANOVA with Kruskal-Wallis test followed by Dunn's test for multiple comparisons were conducted.

a. **Orléans Cohort: Individuals vaccinated with bivalent Original/BA.5 mRNA Pfizer**

Patients ID	Age	Sex	Dose 3 (Pfizer Monovalent)	Dose 4 (Pfizer Monovalent)	Dose 4 or 5 (Pfizer bivalent)	Breakthrough	Days post-bivalent boost			
							before	1M	3M	6M
#1	59	M	Jan-22		Dec-22		0	30	/	/
#2	53	M	Aug-21	Jan-22	Dec-22		0	35	/	/
#3	59	M	Aug-21	Jan-22	Dec-22	Apr-22	0	42	/	/
#4	Unknown	M	Nov-21		Dec-22	Yes (date unknown)	0	53	/	/
#5	61	M	Nov-21		Dec-22	Mar-22	0	26	96	/
#6	57	F	Nov-21		Dec-22	Mar-22	0	36	97	/
#7	36	F	Feb-22		Dec-22	Jan-21	0	37	93	/
#8	69	M	Dec-21		Dec-22		0	45	94	/
#9	49	F	Nov-21		Dec-22	Mar-22	0	35	93	/
#10	40	F	Nov-22		Dec-22	Mar-22	0	28	91	/
#11	31	F	Nov-21		Dec-22	Mar-22	0	27	84	/
#12	41	F	NA		Dec-22	Jan-22	0	29	/	/
#13	62	F	Nov-21	Jun-21	Jan-23		0	/	/	/
#14	67	F	Jun-21	Aug-22	Feb-23	Dec-21	/	/	/	128
#15	71	M	Aug-21	Aug-22	Feb-23	Dec-21	/	/	/	128
#16	50	M	Aug-21		Feb-22		/	/	/	484
#17	61	M	Feb-22		Dec-22	Aug-21	/	/	/	195
#18	67	M	Sep-21		Feb-23	Jan-22	/	/	/	154
#19	55	M	Aug-21	Jan-22	Dec-22		/	/	/	202
#20	76	M	Sep-21		Dec-22	Aug-22	/	/	/	216
#21	62	M	Aug-21	Jan-22	Dec-22	Feb-22	/	/	/	202

b. **Lyon Cohort_Vaccinated with bivalent Original/BA.5 Pfizer**

Patients ID	Age	Sex	Dose 3 (Pfizer Monovalent)	Dose 4 (Pfizer Monovalent)	Dose 4 or 5 (Pfizer bivalent)	Breakthrough	Days post-bivalent boost		
							before	1M	6M
#1	56	F	Nov-21		Dec-22	Jun-22	0	32	207
#2	37	M	Nov-21	Jan-22	Dec-22	Jul-22	0	31	217
#3	61	F	Dec-21	Jan-22	Dec-22	/	0	28	166
#4	42	F	Dec-21		Dec-22	Feb-22	0	32	218
#5	62	F	Oct-21		Dec-22	/	0	30	136
#6	62	F	Nov-21		Dec-22	/	0	28	165
#7	34	M	Nov-21		Dec-22	Jan-22	0	38	152
#8	62	F	Nov-21		Dec-22	/	0	32	/

c. **Orléans Cohort_Breakthrough infection in September 2023**

Patients ID	Age	Sex	Number of Doses	Vaccine	Days post-infection
#1		M	3	Pfizer	50
#2		M	3	Pfizer	42
#3		F	3	Pfizer	14
#4		F	2	Pfizer	39
#5		F	2	Pfizer	24
#6		F	3	Pfizer	20
#7		M	3	Pfizer	10
#8		F	3	Pfizer	25
#9		F	3	Astra + Pfizer	15
#10		M	2	Pfizer	18
#11		F	3	Pfizer	17
#12		F	2	Pfizer + Moderna	14

Table S1

a.

Post third dose		
Sex	Female	13
	Male	8
Age (Median; range)		57; (31-69)
Immunodeficiency		0
Previous COVID-19 (known)		13
1st dose		jan - april 2021
2nd dose		jan - nov 2021
3rd dose		aug 2021 - nov 2022
4th dose		june 2021 - jan 2022
Sampling days post-vaccination (median; range)		373 (25-475)
Cohorts	Orléans (Table S1a)	13
	Lyon (Table S1b)	8

b.

1M post-bivalent (Original/BA.5) dose		
Sex	Female	12
	Male	8
Age (Median; range)		56; (31-69)
Immunodeficiency		0
Previous COVID-19 (known)		13
1st dose		jan - april 2021
2nd dose		jan - nov 2021
3rd dose		aug 2021 -nov 2022
4th dose		nov 2022 - jan 2023
Sampling days post-bivalent boost (median; range)		32 (26-53)
Cohorts	Orléans (Table S1a)	12
	Lyon (Table S1b)	8

c.

6M post-bivalent (Original/BA.5) dose		
Sex	Female	6
	Male	9
Age (Median; range)		62; (34-76)
Immunodeficiency		0
Previous COVID-19 (known)		9
1st dose		janv-21
2nd dose		janv-21
3rd dose		june 2021 - feb 2022
4th dose		feb 2022 - feb 2023
Sampling days post-bivalent boost (median; range)		198 (128-484)
Cohorts	Orléans (Table S1a)	8
	Lyon (Table S1b)	7

d.

0.5M post XBB breakthrough infection		
Sex	Female	8
	Male	4
Age (Median; range)		Unknown
Immunodeficiency		Unknown
Nb of participant with 2 doses		4
Nb of participant with 3 doses		8
Sampling days post-BT (median; range)		19 (10-50)
Cohorts	Orléans (Table S1c)	12

Table S2

Variant	Strain	GISAID ID	Reference
D614G	hCoV-19/France/GES-1973/2020	EPI_ISL_414631	Ref 68
Delta	hCoV-19/France/IDF-APHP-HEGP-20-23-2131905084/2021	EPI_ISL_2029113	Ref 65
BA.1	hCoV-19/Belgium/rega-20174/2021	EPI_ISL_6794907	Ref 52
BA.5	hCoV-19/France/CVL-ChuTo-9800086928/2022	EPI_ISL_13660702	Ref 53
BQ.1.1	hCoV-19/Belgium/Rega-IPP_BA2752i/2022	EPI_ISL_15731524	Ref 34
XBB.1.5	hCoV-19/USA/NY-PRL-2021_0412_01L21/2021	EPI_ISL_1635849	Ref 48
XBB.1	hCoV-19/France/PAC-HCL022171892001/2022	EPI_ISL_15619797	This article
XBB.1.9.1	hCoV-19/France/GES-IPP08594/2023 C2 24/04/2023	EPI_ISL_17419152	This article
XBB.1.16.1	hCoV-19/France/GES-IPP07712/2023 C2 21/04/2023	EPI_ISL_17383796	This article
XBF	hCoV-19/France/IDF-APHP-HEGP-81-10-2332993394/2023	EPI_ISL_17763463	This article
EG.5.1.1	hCoV-09/France/GES-IPP15954/2023	EPI_ISL_17949406	This article
EG.5.1.3	hCoV-19/France/BRE-IPP15906/2023	EPI_ISL_17949372	This article
BA.2.86.1	hCoV-19/France/IDF-IPP17625/2023	EPI_ISL_18221650	This article
JN.1	hCoV-19/France/HDF-IPP21391/2023	EPI_ISL_18363371	This article

Table S3

	Fold decrease versus D614G										
	BA.1	**BA.5**	**BQ.1.1**	**XBB.1**	**XBB.1.5**	**XBB.1.9.1**	**XBB.1.16.1**	**XBF**	**EG.5.1.3**	**BA.2.86.1**	**JN.1**
3 doses of Pfizer	5	5	23	42	35	84	101	64	136	76	101
1M after Original/BA.5 bivalent boost	9	6	50	107	62	150	144	71	141	125	254
6M after Original/BA.5 bivalent boost	4	7	23	31	37	53	75	37	81	90	180
3 weeks after XBB breakthrough infection	2	1	6	8	4	8	9	5	6	10	20

Table S4